ADVANCED MATERIALS INTERFACES Open Access
www.advmatinterfaces.de

Deciphering the Interactions of Carbon Nanotubes and Super P with Silicon and Graphite Active Materials in Silicon-Graphite Negative Electrode-Based Lithium-Ion Batteries

Leyla Ünal, Viviane-Maccio Figgemeier, Felix Weber, Egbert Figgemeier,* and Gebrekidan Gebresilassie Eshetu**

In high-capacity Silicon (Si)-based negative electrodes for Lithium-Ion Batteries (LIBs), conductive additives play a pivotal role for preserving electrical conductivity and electrode integrity, boosting the electrochemical performance. This study presents how defect-mediated Multi-walled Carbon Nanotubes (MWCNTs) impact battery performance when employed as conductive additive material in both high-capacity Si and low-capacity graphite (Gr) electrodes. For benchmarking, state-of-the-art carbon black (Super P) is used. Half-cell test results of MWCNTs-based Si-rich Si/Gr (60/28) blended electrodes exhibit a specific discharge capacity of 534.2 ± 21.1 mAh g^{-1} with a capacity retention of 73.3% at 100th cycle, surpassing Super P-based counterparts, which achieve only 436.1 ± 16.3 mAh g^{-1} and 61.7% retention at the same cycle. However, for Gr-rich Si/Gr (20/68) blended electrodes, the discrepancies in performance and capacity retention between both conductive additives is less significant than in the Si-rich Si/Gr electrode system. Imaging and spectroscopic analyses reveal that the differences in performance originate from the distinctive interactions between the surface functional groups of the conductive additives and those of the active materials. Overall, the findings highlight the critical role of defect-mediated interaction chemistry in MWCNTs in boosting electrochemical performance, offering valuable insights for the design of next-generation LIB electrodes.

1. Introduction

The global demand for Lithium-ion Batteries (LIBs) is surging, fueled by the rapid growth of electro mobility market, and the rising popularity of the integration of renewable energy sources into the energy mix. The market is projected to grow at a compound annual growth rate (CAGR) of 26% between 2020 and 2030.[1] Currently, graphite (Gr) dominates as the negative electrode material in LIBs, owing to its favorable attributes: low (de-)intercalation potential (≤0.2 V vs. Li/Li$^+$), minimal volume expansion during (de-)lithiation (≤10%), high structural stability, low irreversible capacity, and consequently long cycle life (total charge-discharge rounds).[2–8] However, Gr-based LIBs are approaching their practical specific energy density limit (i.e., 250 Wh kg^{-1}),[5] primarily due to the limited theoretical capacity of Gr (372 mAh g^{-1} for LiC$_6$, the maximum lithiated phase). This shortfall prevents them from meeting the

---

L. Ünal, V.-M. Figgemeier, F. Weber, E. Figgemeier
Helmholtz Institute Münster (HI MS)
IMD4
Forschungszentrum Jülich GmbH
Campus Boulevard 89, 52074 Aachen, Germany
E-mail: l.uenal@fz-juelich.de; e.figgemeier@fz-juelich.de

The ORCID identification number(s) for the author(s) of this article can be found under https://doi.org/10.1002/admi.202500503

DOI: 10.1002/admi.202500503

F. Weber, E. Figgemeier, G. G. Eshetu
Center for Ageing
Reliability and Lifetime Prediction of Electrochemical and Power Electronic Systems (CARL)
RWTH Aachen University
Campus Boulevard 89, 52074 Aachen, Germany
E-mail: gebrekidan.eshetu@isea.rwth-aachen.de

E. Figgemeier
Jülich Aachen Research Alliance
JARA-Energy
52425 Jülich, Germany

G. G. Eshetu
Department of Material Science and Engineering
Mekelle Institute of Technology—Mekelle University
1632 Tigray, Ethiopia

stringent demands of emerging advanced battery applications.[2–4,9] In this realm, lithium alloying chemistries represent as the most appealing alternatives, offering higher capacities compared to traditional intercalation materials. Among various alloying candidates, Silicon (Si) stands out as a highly potent electrode material due to its remarkably high theoretical specific capacity of 3590 mAh g^{-1} (for $Li_{15}Si_4$ at room temperature), nearly 10 times that of graphite (372 mAh g^{-1})[10] while also being earth-abundant, low-cost, environmentally benign, and operating at a suitable potential (≤0.4 V vs. Li/Li^+), making it a leading contender for future LIBs [4,11,12] However, several critical challenges remain unresolved, including: 1) the anisotropic volume swelling of Si (≥ 280%) during (de-)lithiation induces mechanical stress, and structural degradation, leading to crack formation and pulverization of Si particles and growth of an unstable and thick Solid Electrolyte Interphase (SEI) layer that impedes efficient Li-ion transport, and thus affects the cycling performance, Coulombic Efficiency (CE), and rate capability;[5,9,12,13] 2) much lower intrinsical electronic conductivity ($\sigma_e < 10^{-5}$ S cm^{-1}) and Li-ion diffusion rate ($D_{Li}{}^+$, 10^{-14} –10^{-13} cm^2 s^{-1}) in high-purity Si compared to that of Gr (σ_{e-}, 10–10^4 S cm^{-1}; $D_{Li}{}^+$, 10^{-9} cm^2 s^{-1}); and 3) crystallization of Si during cycling.[5] To overcome these obstacles, various strategies have been proposed, including combining Si particles with carbon-based materials in the form of blended or composite, incorporation of a small dose of electrolyte additives and polymeric binders.[5] In addition, optimizing conductive additives has emerged as a key approach to mitigate the fundamental limitations of Si-based negative electrodes. [3,5] They aid in the formation of flexible structures that can withstand volume expansion, boost ion and electron diffusivity, and promote the formation of a stable and efficient SEI layer. Among various carbonaceous materials, Carbon Nanotubes (CNTs), in both single- and multi-walled forms, are gaining popularity as electrode conductive additive materials in the negative electrodes of LIBs due to their unique properties, such as exceptional electronic conductivity, remarkable mechanical strength, and high flexibility. This is especially attractive for electrodes that undergo significant volume changes and exhibit low electrical conductivity, as in Si-based electrodes.[2,3,14–16] However, MWCNTs produced by chemical vapor deposition, arc discharge, and laser ablation are rarely obtained in pure form; they typically contain intrinsic defect sites, vacancies, and oxygen-containing functional groups (e.g., —OH, —COOH, —C═O), emanating from the synthesis or subsequent purification, covalent functionalization, and non-covalent surface modifications.[17,18] Although commonly viewed as defects, these sites confer chemical reactivity, promoting interactions with other components during electrode slurry preparation and/or enhancing dispersion in polar media.[18,19] For instance, these functional moieties can interact with the oxide-rich surface of Si particles through hydrogen bonding and covalent coupling, thereby strengthening interfacial contact that impacts the electrode stability.[20,21] The novelty of this work lies in demonstrating that defect-rich MWCNTs function not merely as conductive additives but as interfacial mediators. Our study shows that their defective structure and surface chemistry significantly influence the electrochemical behaviour of pure Si and Si-rich negative electrodes-based battery cells. For benchmarking, pure Gr and Gr-rich Si/Gr negative electrodes-based battery cells are evaluated. For comparison, state-of-the-art Super P as a conductive additive both in Gr and Si-based battery cells is tested under the same electrode formulation, cell configuration and conditions. Contrary to expectations that defect-rich MWCNTs reduce electrical conductivity,[19,22–25] this study demonstrates that defective MWCNTs suppress battery degradation and improve rate capability in Si-rich Si/Gr negative electrode-based cells. This improvement arises from the interplay between MWCNTs surface chemistry (defects and functional groups) and Si through interfacial chemical bonding, as well as favorable electrode structural evolution during cycling. In contrast, Super P-based electrodes exhibit accelerated degradation and limited rate capability due to their morphology and surface chemistry which lead to reduced mechanical stability, highlighting the critical impact of the conductive additive's nature. Our work addresses these by correlating ATR-FTIR and RAMAN spectroscopies before and after cycling of MWCNTs- and Super P-containing negative electrodes. Overall, this study underscores the crucial role of defect-rich MWCNTs and the need for in-depth understanding of their surface chemistry to advance high-energy density Si-based LIBs.

2. Results and Discussion

2.1. Material Characterization and Half-Cell Tests

SEM images show a thread-like structure of MWCNTs with randomly oriented and entangled tubes, a common shape in CNT samples where the tubes are densely packed (**Figure 1**a,b).[26–28] Each tube varies in length and thickness, ranging from 0.1 to 10 µm; with outer diameters in the range of 10–15 nm as provided by the supplier ARKEMA. The specific surface area of the MWCNTs is 175 m^2 g^{-1} (Graphistrength C100, powder material).[29] According to supplier, the same MWCNTs material was used in the production of the dispersion. In contrast, Super P shows a dot-like particle structure that tends to aggregate into irregular clusters (Figure 1c,d). This powdery structure exhibits an average particle size of 40 nm and a specific surface area of 62 m^2 g^{-1} (provided by supplier IMERYS TIMCAL) and distinctly differs from the entangled filamentous morphology of MWCNTs.

SEM images of pure Gr negative electrode show flake-like Gr particles (average particle size of 22.9 µm) that are extensively wrapped by an intricate network of MWCNTs (**Figure 2**a,b). In particular, the Gr edges are partially covered by MWCNTs (Figure 2b). Whereas, Super P aggregates are observed on specific areas of the Gr particles (Figure 2c,d). The Si-alloy particles vary in size, ranging from 0.9 to 24 µm. This size disparity affects their interaction with MWCNTs, showing some Si-alloy particles become fully encapsulated by thread-like MWCNTs, as illustrated in SEM images of Gr-rich Si/Gr (20/68) and Si-rich Si/Gr (60/28) negative electrodes (Figure 2e,f,i,j). Conversely, Super P particles are primarily located between the active particles (Figure 2g,h,k,l). This is also evident with pure Si negative electrode, where MWCNTs are convoluted tightly between Si-alloy particles (Figure 2n), whereas Super P is distributed across the Si-alloy particles (Figure 2p). All these demonstrate the different affinities and degrees of interaction between the conductive additives and electrode active particles.

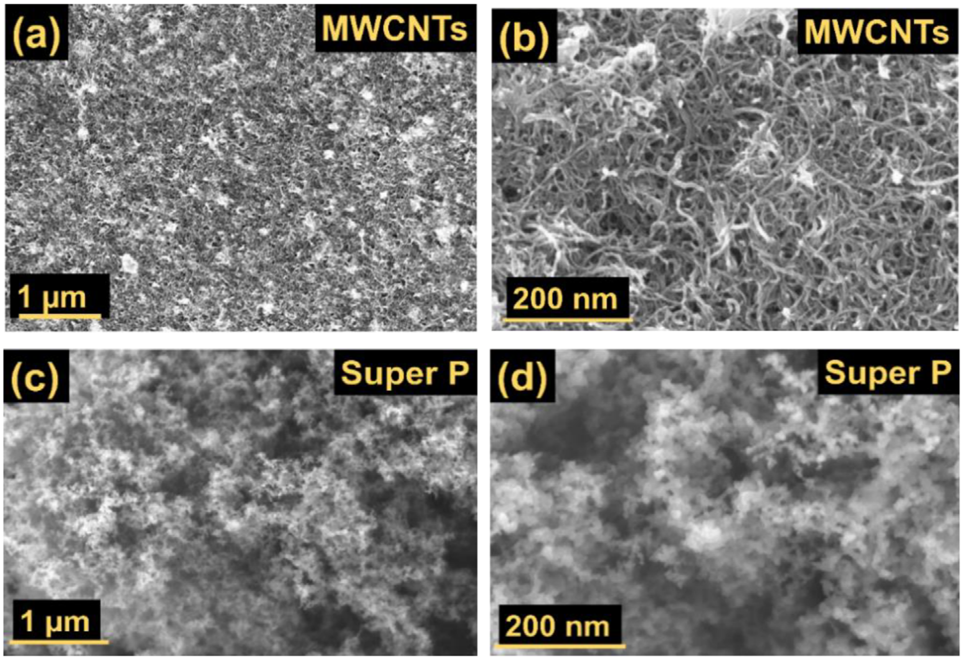

Figure 1. SEM images of a, b) MWCNTs and c, d) Super P conductive agents.

To gain insights into the structural characteristics and surface composition of pristine materials and the as-prepared (non-cycled) negative electrodes, a comparative analysis utilizing ATR-FTIR and RAMAN spectroscopy was conducted. Figure 3 illustrates ATR-FTIR spectra of pristine materials used for negative electrode fabrication as well as the as-prepared negative electrodes.

The ATR-FTIR spectrum of pristine Gr shows a peak at 1610 cm^{-1}, which is characteristic of the C=C bond stretching of the benzene ring present in the graphene layers (**Figure 3a**).[30] In addition, the peaks at 810 and 670 cm^{-1} are ascribed to C—H bending vibrations in aromatic structure in Gr, which seems also be present in Super P (Figure 3a).[2,3,31,32] Similar features appear in the pristine Si-alloy material that consists of amorphous Si particles finely distributed within a crystalline iron disilicide ($FeSi_2$) and carbon matrix.[33–37] Furthermore, the broad peak at ≈1300 cm^{-1} represents Si–O or/and Si–O–Si groups of the Si surface.[38,39] The ATR-FITR spectrum of pristine MWCNTs material exhibits a peak at 1720 cm^{-1} (—C=O), a sharp and broad absorption peak at 1564 cm^{-1} (–COO^-), and a broad peak at 970 cm^{-1} (–C–O), indicating the presence of oxygenated functional groups on the surface. Peaks in the range of 1415–1300 cm^{-1} correspond to aliphatic compounds (–CH_2, –CH_3) that can be assigned to bending vibrations (Figure 3a).[40–42] This evidence shows that MWCNTs have polar and non-polar functional groups on their surface. On the contrary, Super P contains fewer functional groups compared to MWCNTs (Figure 3a). Such surface functionalities may dictate the nature and degree of interaction with that of Gr and Si active materials.

The ATR-FTIR spectra of the as-prepared negative electrodes display peaks related to various functional groups, such as carbonyl (—C=O, 1800 – 1740 cm^{-1}), alkene (—C=C, 1680–600 cm^{-1}), carboxylate anion (—COO^-, ≈1580 cm^{-1}), aliphatic (–CH_2, –CH_3, 1400–1300 cm^{-1}) as well as siloxane, silanol (Si–O–Si, Si–OH, 1070–900 cm^{-1}) groups.[43–48] A more intricate group composition is observed in the Si/Gr blend compared to the reference systems (pure Gr and Si-based negative electrodes), which is attributed to the presence of electrode conductive additives and polymeric binders used during the electrode fabrication process (Figure 3c,d). In the reference negative electrodes, only LiPAA and CMC were used for Si and Gr-based negative electrodes as per established literature.[49] The RAMAN spectra and estimated R values (I_D/I_G) are further shown in **Figure 4**

The RAMAN spectra exhibit three features: 1) the D band (≈1350 cm^{-1}), associated with structural defects, disorder or irregularities, 2) the G band (≈1580 cm^{-1}), ascribed to well-ordered graphitic structure, and 3) the 2D band (≈2700 cm^{-1}), which reflects the number of graphene layers, and provides insights into their number/quality of layers, as defects at the edges, vacancies and functional groups can influence the characteristics of the 2D band.[2,3,50] Moreover, the intensity ratio of the D and G bands ($R = I_D/I_G$) provides crucial information about the material's degree of structural order or disorder. A higher degree of disorder results in an increased R value, indicating high defect density.[2,3,51,52] The Si-alloy exhibits an amorphous structure, evidenced by the broad 400 – 500 cm^{-1} peak (Si_a). The RAMAN spectrum further confirms carbon by-products in Si-alloy through distinct D and G bands (Figure 4a). The estimated R values for MWCNTs and Super P are 1.4 and 1.05 (Figure 4b), indicating that the MWCNTs material exhibits a higher defect density than Super P. Regarding active materials, the Si-alloy material shows a higher defect density (R ≈ 0.73) than Gr (R ≈ 0.09). On the other hand, an intense D band is observed for all MWCNTs-containing negative electrodes, indicating a higher defect density compared to their Super P-containing counterparts, inher-

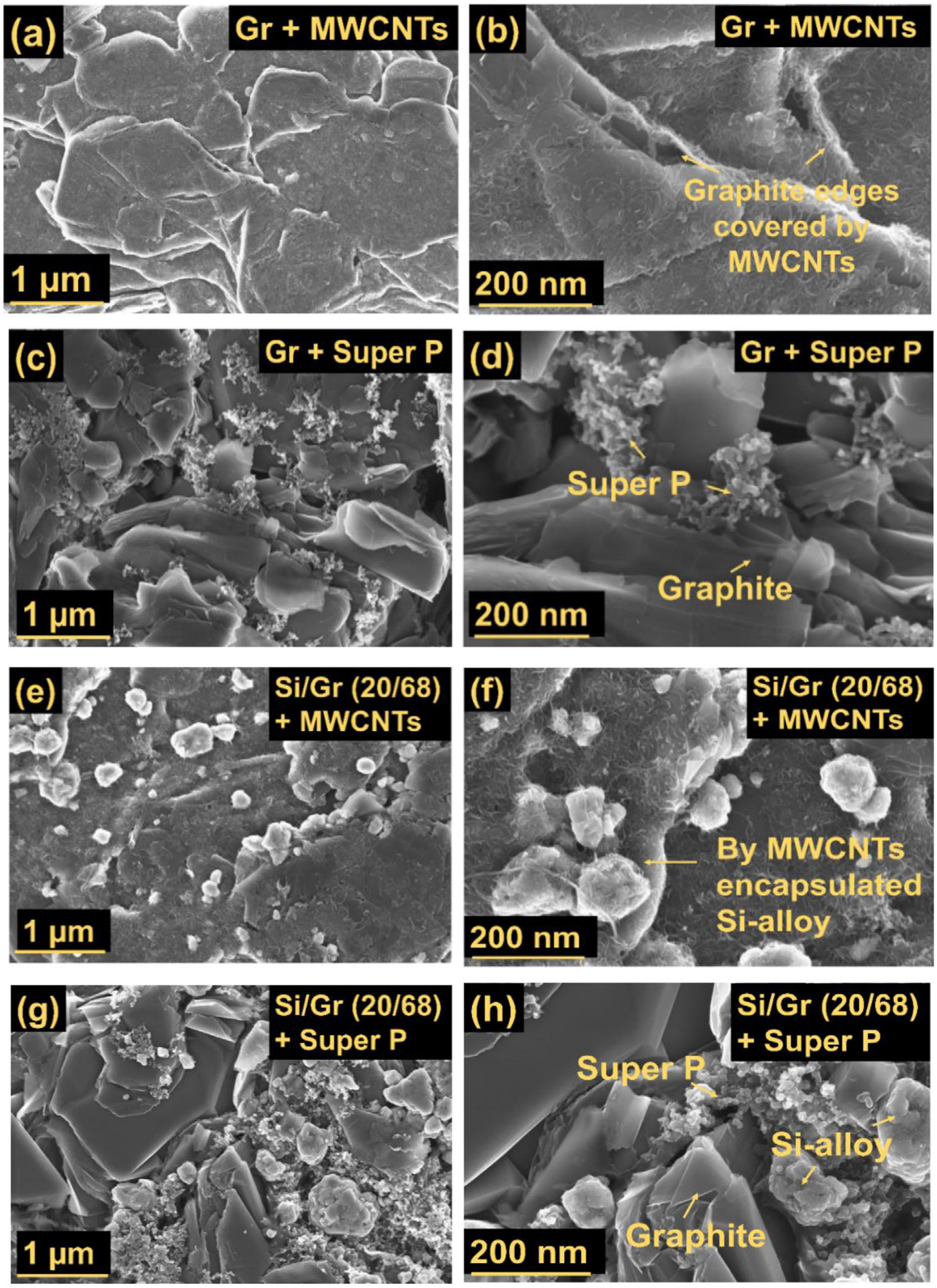

Figure 2. SEM images of the as-prepared a, b) Gr + MWCNTs; c, d) Gr + Super P; e,f) Gr-rich Si/Gr (20/68) + MWCNTs; g,h) Gr-rich Si/Gr (20/68) + Super P; i,j) Si-rich Si/Gr (60/28) + MWCNTs; k,l) Si-rich Si/Gr (60/28) + Super P; m,n) Si + MWCNTs, and o,p) Si + Super P negative electrodes.

ited from the MWCNTs material itself (Figure 4c–f). An increase in Si-alloy content in Si/Gr blend results in a higher defect density as depicted by an elevated value of R in MWCNTs-based electrodes, suggesting a potential interaction between MWCNTs and Si (**Figure** 11e). However, such a trend is not observed with Super P as the R value remained relatively constant in both pure Gr and Si/Gr-based negative electrodes. A notable increase in the R value is observed only in the case of Si + Super P negative electrode, though this increase is also less pronounced compared to MWCNTs-based one (Figure 11e).

The Si surface features various functional groups such as Silanol (–Si–OH), Siloxane (Si–O–Si), and native passivation film, i.e., Silicon dioxide (SiO_2) groups.[53,54] The defect-rich MWCNTs exhibit functional groups such as carboxyl (–COOH) and carbonyl (—C=O) groups as shown in the ATR-FTIR spectrum (Figure 3a). Interactions such as hydrogen bonding can occur between silanol (Si–OH) groups of the Si/Si-rich active material and carboxyl (–COOH) groups on MWCNTs. Specifically, during the slurry mixing step, mechanical forces may induce local heating or stress that can promote covalent bonding via

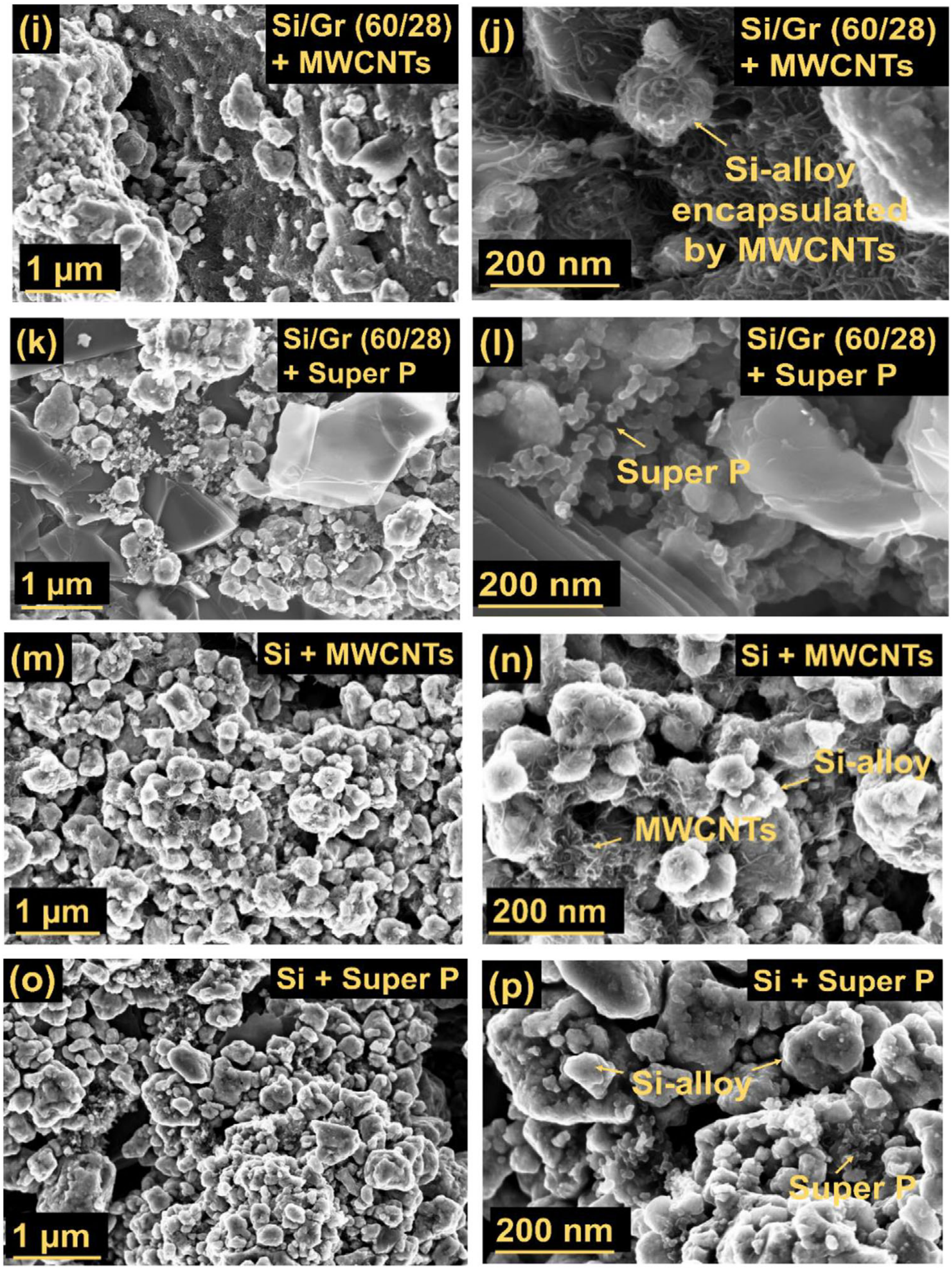

Figure 2. *Continued*

condensation/esterification and silanization reactions between Silanol groups (–Si–OH) and the –COOH or –OH groups on the MWCNTs as shown in **Figure** 5.

These reactions can tailor the interfacial reactions between MWCNTs and Si, enhancing their adhesion and contributing to structural stability in composite electrode materials. In contrast, Gr interacts via weak van der Waals forces between layers, such as weak π-π stacking, rather than forming strong covalent bonds. Consequently, the interaction between MWCNTs and Gr is much weaker as compared to the binding between MWCNTs and Si.

Unlike Si, Gr is characterized by its highly crystalline and ordered structure, enabling Li-ion intercalation between its well-defined graphene planes. Although the defects on MWCNTs offer extra sites for Li-ion storage, these additional sites can often lead to irreversible side reactions (such as excessive SEI formation and Li immobilization) that limit their effective contribution to obtainable capacity. Consequently, the overall capacity of the electrode remains dominated by Gr's intercalation mechanism, with the MWCNTs or Super P primarily contributing to a robust electrical contact and structural stability rather than to enhance

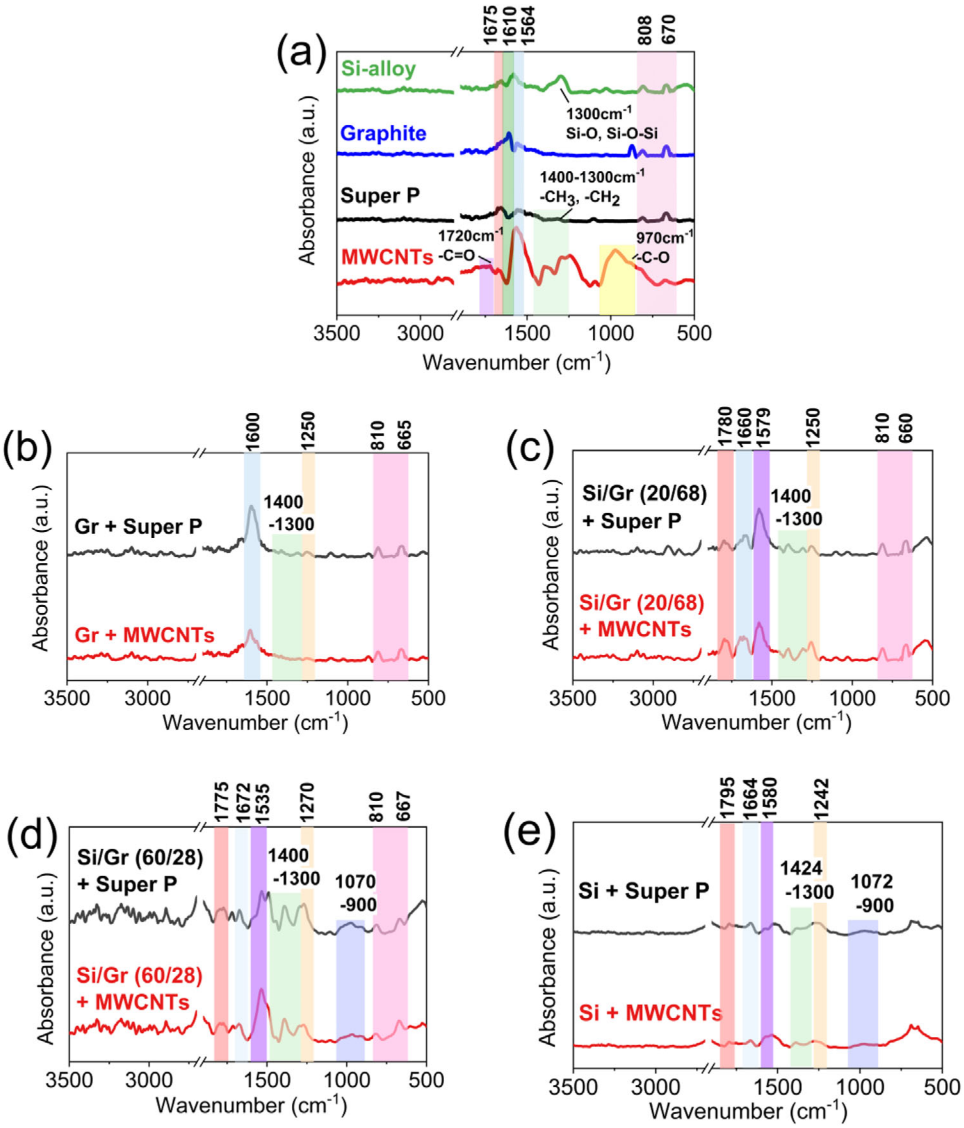

Figure 3. ATR-FTIR spectra of: a) pristine materials used for negative electrode fabrication and of as-prepared; b) Gr + MWCNTs and Gr + Super P; c) Gr-rich Si/Gr (20/68) + MWCNTs and Gr-rich Si/Gr (20/68) + Super P; d) Si-rich Si/Gr (60/28) + MWCNTs and Si-rich Si/Gr (60/28) + Super P; e) Si + MWCNTs and Si + Super P negative electrodes.

capacity. This is clearly illustrated in the voltage profiles of Gr negative electrodes-based lithium-ion cells in **Figure 6a**.

They exhibit plateaus within the range of 0.2 to 0.05 V vs. Li/Li$^+$, corresponding to the formation of various Li-Gr intercalation compounds, e.g., Li_xC_{32}, Li_xC_{12}, and Li_xC_6.[55] No significant differences are observed in the voltage profiles between pure Gr and Gr-rich Si/Gr blend negative electrodes with MWCNTs or Super P (Figure 6a,b), suggesting that the electrochemical response is predominantly governed by the Gr component. In contrast, for Si-rich Si/Gr and pure Si negative electrode systems (Figure 6c,d), a different behaviour is seen. Specifically, the initial lithiation process with MWCNTs results in a higher degree of lithium insertion, which enhances the initial capacity by forming a Li_xSi-alloy. After 100 cycles, the Si-rich Si/Gr (60/28) + Super P electrode shows a significantly lower lithiation capacity compared to its MWCNTs counterpart (Figure 6c). This trend is further pronounced in the pure Si negative electrode: The voltage curves of the pure Si negative electrode clearly highlight the beneficial effect of MWCNTs in the presence of Si, exhibiting nearly twice the lithiation capacity at 100th cycle compared to the Super P counterpart (Figure 6d). **Figure 7** shows the half-cell cycling outcomes of MWCNTs and Super P-containing negative electrode-based cells.

All battery cells exhibit fluctuations in CE, which is due to excess lithium reservoir in a half-cell set-up, leading to continuous parasitic side reactions and generating electrochemically inactive by-products by irreversible Li-ion consumption.[55] The cycling results show a higher ICE for Gr + MWCNTs (≈89.1%) as compared to its counterpart with Super P (≈68.6%) (**Table 1**).

However, the cycling performance of Gr + MWCNTs displays almost similar or only a slight decrease in specific discharge capacity and capacity retention at the 100th cycle

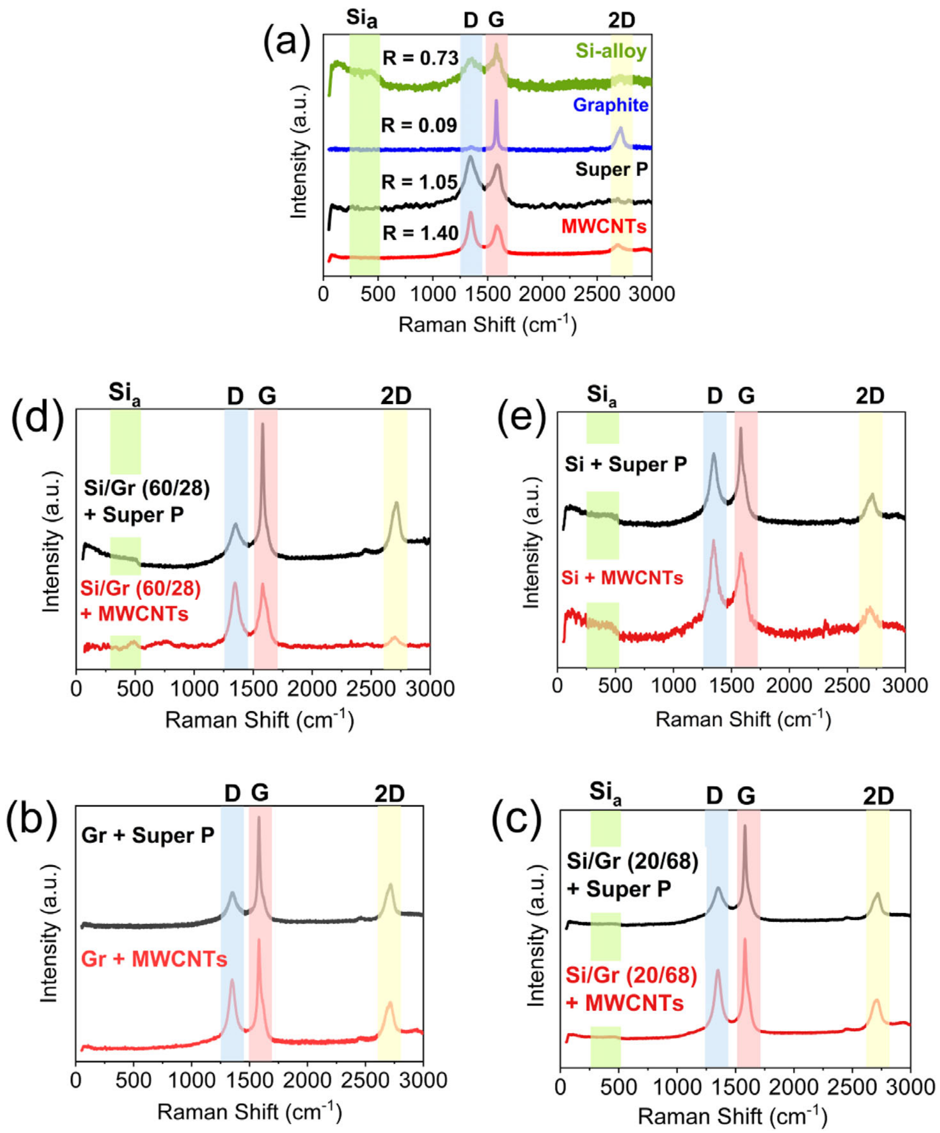

Figure 4. RAMAN spectra of: a) materials used for negative electrode fabrication and estimated R (ID/IG) values. RAMAN spectroscopy results of the as-prepared; b) Gr + MWCNTs and Gr + Super P; c) Gr-rich Si/Gr (20/68) + MWCNTs and Gr-rich Si/Gr (20/68) + Super P; d) Si-rich Si/Gr (60/28) + MWCNTs and Si-rich Si/Gr (60/28) + Super P; e) Si + MWCNTs and Si + Super P negative electrodes.

(349.7 ± 7.4 mAh g^{-1} and ≈97.4%), compared to Gr + Super P (360.3 ± 7.1 mAh g^{-1} and ≈98%) (Figure 7a, Table 1). As shown in the SEM images, MWCNTs form a conductive network covering the Gr surface (Figure 2a,b), through the passivation of reactive sites of Gr, specifically at edges where electrolyte decomposition predominantly occurs.[56] This discerning coverage by MWCNTs may reduce the high irreversible Li-ion consumption. In contrast, Super P, which is a quasi-spherical, isotropic carbon particle that forms discrete contact points that do not cover Gr edges (Figure 2c,d), leading to higher irreversible Li-ion consumption and consequently to a lower Initial Coulombic Efficiency (ICE). However, once the SEI layer is formed for both cases, it acts as a stable passivation layer, which probably minimizes further irreversible reactions during subsequent cycles. As a result, the long-term cycling performance becomes similar for both electrode systems regardless of the slight difference in ICE.

For the Si/Gr (20/80) blend negative electrodes, the ICE is found to be lower for MWCNTs-based design (≈85.5%) compared to the electrode system incorporating Super P (≈87.1%). This could be related to the initial consumption of a large amount of Li-ion. However, despite lower ICE, MWCNTs-containing Gr-rich Si/Gr (20/68) electrode cell exhibits superior electrochemical performance and improved capacity retention (448.1 ± 10.5 mAh g^{-1} and ≈87.9% at the 100th cycle) compared to its Super P counterpart (406.3 ± 14.6 mAh g^{-1} and ≈83.4% at the 100th cycle). Furthermore, with an increase of Si content in the Si/Gr blend, incorporation of MWCNTs results in a more enhanced reversible specific capacity of 534.2 ± 21.1 mAh g^{-1} and an improved capacity retention of ≈73.3% at the 100th cycle,

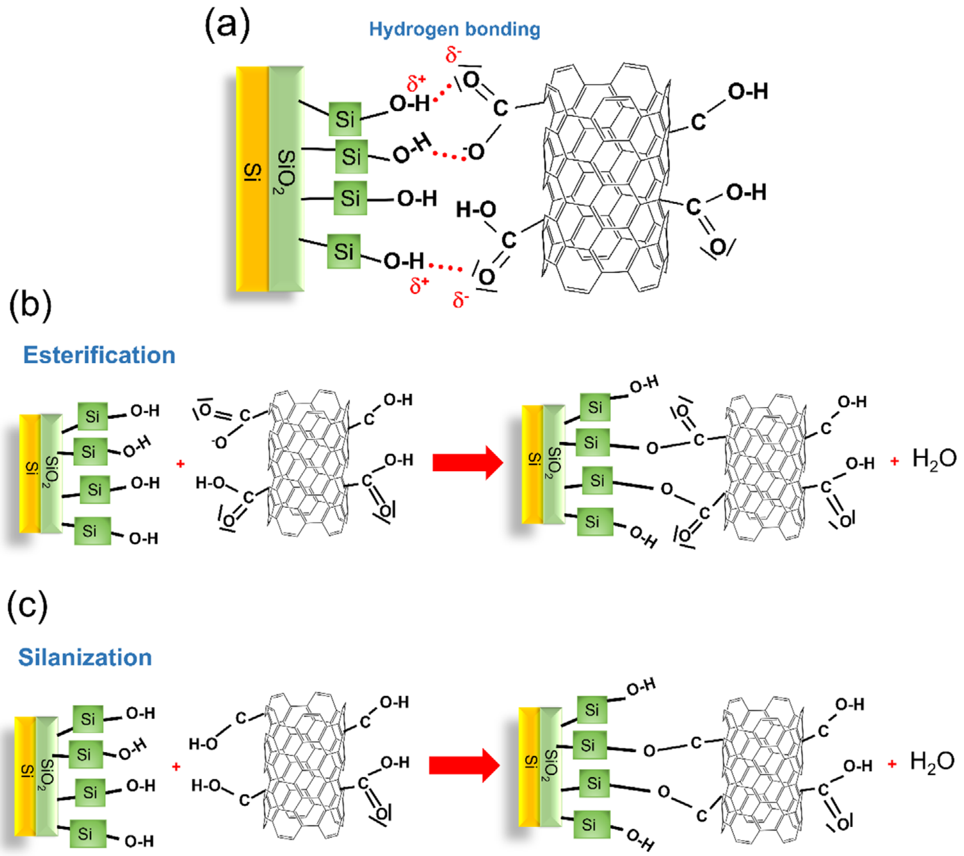

Figure 5. Possible reactions between surface functional groups of Si-alloy surface (–Si–OH) and those on MWCNTs (–COOH, –COO- and –COH).

compared to Super P-based battery cell, which exhibits a decline in cycling performance and capacity retention of 436.1 ± 16.3 mAh g^{-1} and ≈61.7%, respectively. These results evidence that despite lower ICE due to high Li-ion consumption during the SEI formation and other competing side reactions during the initial cycles, MWCNTs form a stable interphase resulting in an enhanced cycling performance and capacity retention (Figure 7b,c). In line with the above trend, the non-blended Si + MWCNTs negative electrode achieved a capacity of 710.8 ± 19.9 mAh g^{-1} with ≈71.7% of capacity retention at the 100th cycle. In contrast, Si + Super P shows poorer performance with a capacity of 439.0 ± 64.8mAh g^{-1} and only ≈58.8% capacity retention at the 100th cycle, once again showing the positive impact of the reaction chemistry between the functional groups on MWCNTs and Si, including improving structural integrity and SEI stabilization. Table 1 summarizes the obtained electrochemical performance data for all electrode formulations.

To provide a comprehensive overview of the capacity degradation for each negative electrode system, the lithiation capacity loss (C_{loss}, Equation 1) from the 1st to 100th cycle was evaluated and is presented in **Figure 8**.

$$C_{loss} = \frac{discharge\ capacity\ (1st\ cycle) - discharge\ capacity\ (100th\ cycle)}{discharge\ capacity\ (1st\ cycle)} \; x\ 100\% \qquad (1)$$

The lithiation capacity loss with MWCNTs containing Si negative electrode–based battery cells is significantly lower than that of Super P counterpart, particularly with a higher percentage of Si as in Si-rich Si/Gr (60/28) blended (i.e., ≈27% with MWCNT vs. ≈38% with Super P) and pure Si (≈28% for MWCNTs *vs.* ≈47% for Super P) negative electrode-based battery cells. In summary, the obtained results clearly demonstrate that MWCNTs endow specific features that sustain capacity, and its effect gets more pronounced in Si-rich Si/Gr and pure Si negative electrodes. The difference in performance between MWCNTs and Super P-containing electrodes lies in the peculiar interaction of their functional groups with that of Si active materials emanating from the natural oxide filmand other different functional groups, defects, etc., and their intrinsic physico-chemical properties.

2.2. Post-Mortem Analysis

To investigate the morphological changes in MWCNTs and Super P-containing negative electrodes after cycling (charge/discharge), SEM images are presented in **Figure 9**. Electrodes cycled vs. Li/Li^+ in half-cell set-up were extracted at the 30th discharge (lithiated) cycle for characterization.

As depicted in Figure 9a,b, the surface of cycled Gr + MWCNTs negative electrode shows a blurred appearance and the MWCNTs that were visible in the as-prepared state (Figure 2b) are no longer

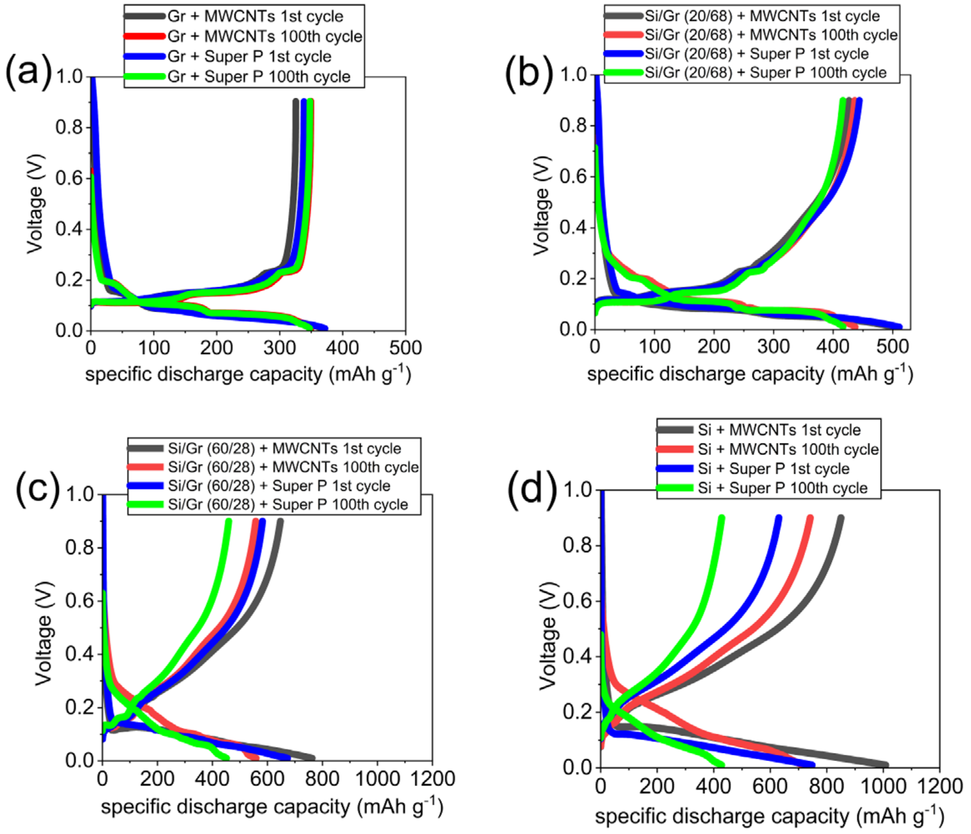

Figure 6. Voltage profiles (1st and 100th cycle) of a) Gr + MWCNTs and Gr + Super P, b) Gr-rich Si/Gr (20/68) + MWCNTs and Gr-rich Si/Gr (20/68) + Super P, c) Si-rich Si/Gr (60/28) + MWCNTs and Si-rich Si/Gr (60/28) + Super P, d) Si + MWCNTs and Si + Super P negative electrode-based half-cells.

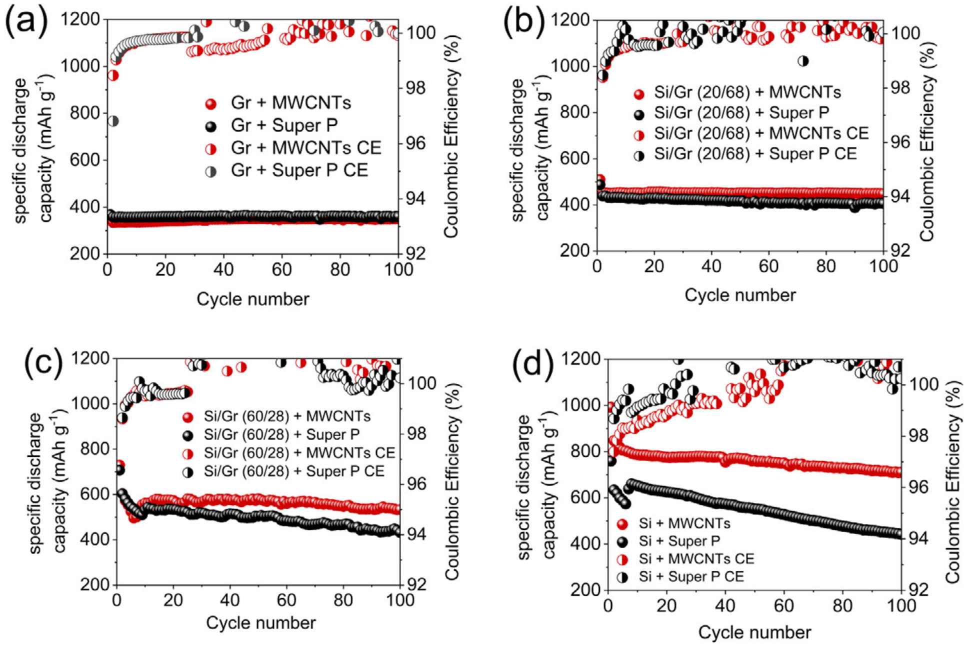

Figure 7. Half-cell cycling results of: a) Gr + MWCNTs and Gr + Super P; b) Gr-rich Si/Gr (20/68) + MWCNTs and Gr-rich Si/Gr (20/68) + Super P; c) Si-rich Si/Gr (60/28) + MWCNTs and Si-rich Si/Gr (60/28) + Super P; d) Si + MWCNTs and Si + Super P negative electrodes.

Table 1. Summary of obtained electrochemical performance data of cycled negative electrodes in a half-cell set-up.

Negative Electrodes	Initial CE [%]	Specific discharge capacity 100th cycle [mAh g^{-1}]	Capacity retention 100th cycle [%]
Gr + MWCNTs	89.1	349.7 ± 7.4	97.4
Gr + Super P	68.6	360.3 ± 7.1	98.0
Si/Gr (20/68) + MWCNTs	85.5	448.1 ± 10.5	87.9
Si/Gr (20/68) + Super P	87.1	406.3 ± 14.6	83.4
Si/Gr (60/28) + MWCNTs	84.7	534.2 ± 21.1	73.3
Si/Gr (60/28) + Super P	86.2	436.1 ± 16.3	61.7
Si + MWCNTs	84.3	710.8 ± 19.9	71.7
Si + Super P	83.9	439.0 ± 64.8	58.8

discernible. This blurred structure likely result from the deposition of electrolyte decomposition products during (de-)lithiation, as the loss of well-defined graphite edges indicates the formation of a surface layer or modification of the graphite surface. In contrast, Super P particles remain clearly visible (Figure 9c,d). A similar behaviour is evident in both blended and pure Si negative electrodes. The surface of the cycled Gr-rich Si/Gr (20/68) + MWCNTs electrode exhibits an irregular,jagged surface morphology (Figure 9e,f). On the contrary, there is no such irregularity with Super P particles; instead, they remain distinctly visible (Figure 9g,h). In cycled Si-rich Si/Gr (60/28) + MWCNTs and pure Si + MWCNTs negative electrodes, a blurred film is observed between the Si-particles (Figure 9k,o). Conversely, Super P particles remain detectable (Figure 9m,q). Furthermore, the surface of cycled Si + Super P negative electrode reveals significant cracking (Figure 9p), which is notably absent in the cycled Si + MWCNTs electrode (Figure 9n). As illustrated in **Figure 10**, during the charge/discharge process, Si-alloy particles undergo significant volume changes, eventually leading to cracking and fragmentation. MWCNTs mitigate this effect by forming conductive bridges between the broken Si-alloy particles, maintaining structural integrity and electrical connectivity(Figure 10a). In contrast, Super P can't form such connections, leading to larger cracks and loss of contact between particles as observed in SEM images (Figure 9p), which could be among the reasons into why the performance deteriorates over long-term cycling, including in the case of internal pulverization as depicted in Figure 10.

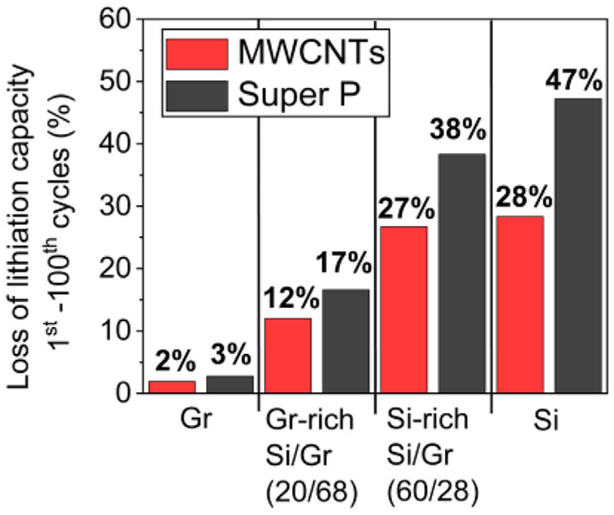

Figure 8. Comparison of lithiation capacity loss from the 1st to 100th cycle for MWCNTs- and Super P-containing as electrode conductive additives.

Another critical factor could be the interaction between defect-rich MWCNTs and binders such as CMC and LiPAA, which differs markedly from Super P due to their surface chemistry and functional groups. The carboxyl and carbonyl groups on MWCNTs can form hydrogen and covalent bonds with the –COOH/–OH groups of CMC and LiPAA, leading to stronger adhesion, better dispersion, and improved mechanical integrity of the electrode film.[57,58]

In contrast, the relatively amorphous, hydrophobic, and chemically inert surface of Super P shows weak interactions with aqueous binders, providing minimal mechanical reinforcement. By comparison, MWCNTs improve film elasticity, reduce cracking and delamination in Si-rich systems, and lower interfacial resistance through stronger binder interactions. In our previous work, Si/Gr electrodes with MWCNTs showed no cracks under bending, unlike their Super P-based counterparts.[3]

To gain a more detailed insight into the chemical makeup, structure, and other functional properties of the SEI formed on MWCNTs and Super P-containing negative electrodes, ATR-FTIR measurements were conducted. Figure 11 shows the ATR-FTIR spectra of cycled MWCNTs and Super P-containing negative electrodes, exhibiting characteristic absorption peaks at ≈1764 ($-C{=}O$), 1570 – 1580 ($-COO^-$), 1450 – 1300 ($-CH_2$, $-CH_3$), 1190, 1080 (C–O–C, –C–O), 830 – 721 cm^{-1} ($-OCO_2$).

The broad and intense peak at ≈1764 cm^{-1} is attributed to the C═O stretch of ester Ethylene Carbonate (EC) or from SEI compounds bearing such bonding, as further supported by the presence of a peak at 1190 cm^{-1} (–C–O–C).[3,59–67] Peaks at 1570 cm^{-1} ($-COO^-$), 1450 – 1300 cm^{-1} ($-CH_2$, $-CH_3$), 829 – 720 cm^{-1} ($-OCO_2$) corresponding to lithium alkyl carbonates such as CH_3OCO_2Li, $[CH_2OCO_2Li]_2$, and $CH_3CH_2OCO_2Li$.[68,69] The peak at 1570 cm^{-1} ($-COO^-$) suggests the existence of carboxylate groups, which may originate from binders used for electrode preparation (e.g., LiPAA/CMC in this study) and SEI compounds. It is important to note that the ATR-FTIR analysis did not reveal significant differences between cycled MWCNTs and Super P-containing Gr and Gr-rich Si/Gr (20/68) negative electrodes. However, distinct differences are observed in cycled Si and Si-rich Si/Gr (60/28) systems in that the intensity of the C═O peak at ≈1764 cm^{-1} is notably lower for

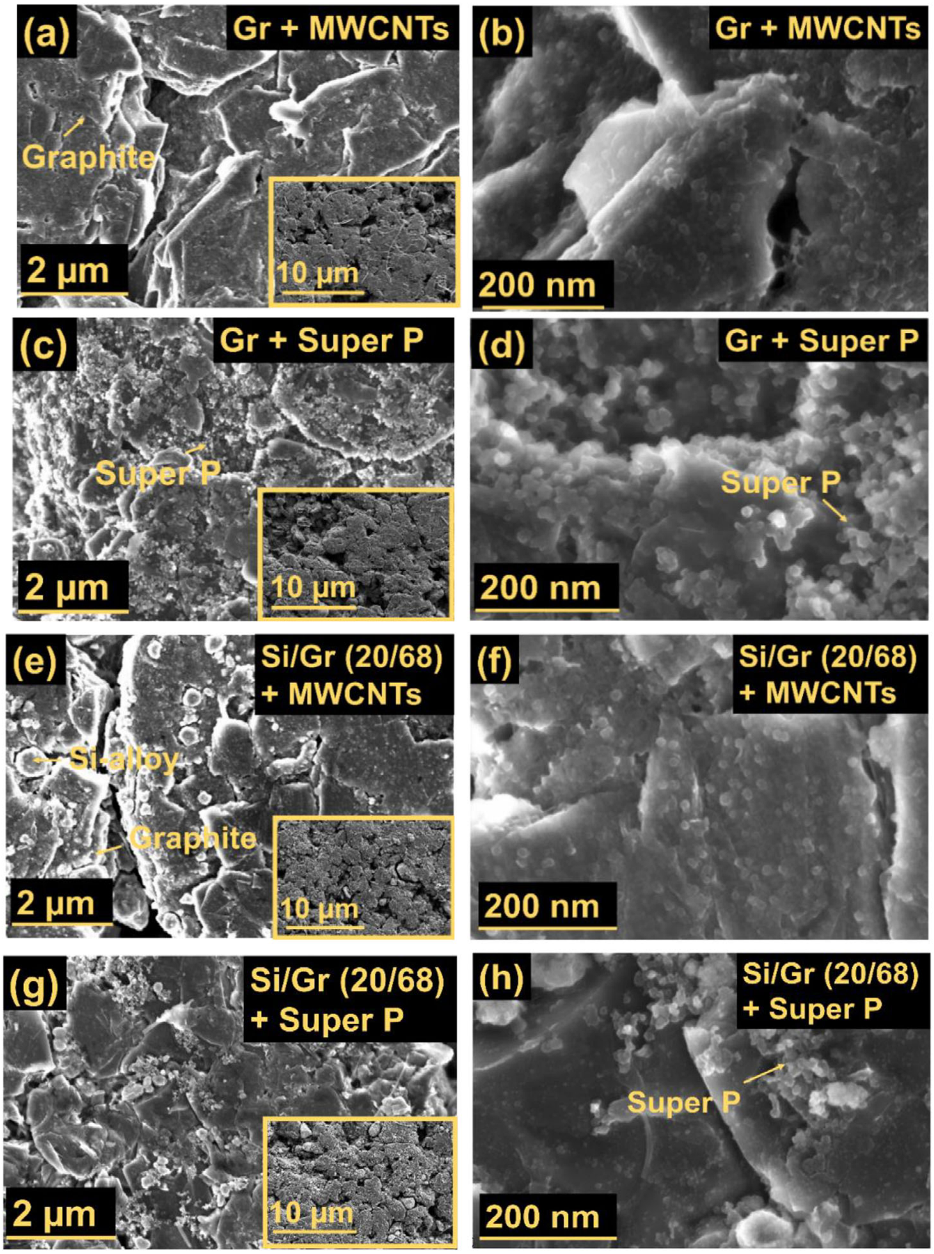

Figure 9. SEM images of cycled (vs. Li/Li+, 30th cycle): a, b) Gr + MWCNTs; c, d) Gr + Super P; e, f) Gr-rich Si/Gr (20/68) + MWCNTs; g, h) Gr-rich Si/Gr (20/68) + Super P; i, j) Si-rich Si/Gr (60/28) + MWCNTs; k, l) Si-rich Si/Gr (60/28) + Super P; m, n) Si + MWCNTs; and o, p) Si + Super P negative electrodes.

cycled Si-rich Si/Gr (60/28) + Super P compared to cycled Si-rich Si/Gr (60/28) + MWCNTs (Figure 10c). In contrast, a well-defined SEI structure is observed on cycled Si-rich Si/Gr (60/28) + MWCNTs, with the emergence of a new peak at 900 cm$^{-1,}$ which is absent in its Super P counterpart (Figure 11c). This peak could be linked to C–H out-of-plane bending vibrations or C–O stretching vibration in $[LiOCO_2CH_2]_2$.[70] The degradation of the passivation layer becomes more intense in cycled Si + Super P and the large broad peak at ≈1764 cm^{-1}, typically present in all cycled negative electrodes, is absent (Figure 11d). Additional evidence of surface species in Si + Super P-based cells is found in the broad peak between 1250–890 cm^{-1}, likely arising from overlapping vibrational modes associated with Si–O–Si/Si–O, C–O–C, and salt degradation products such as PF_6^- or PO_2F_2 groups.[71–74] The appearance of these broad peaks during cycling may signal ongoing electrolyte decomposition, which could be correlated with capacity fade and poor long-term performance, as reflected in the electrochemical performance data (Figure 7d). Furthermore, large cracks are seen in the SEM images of cycled Si + Super P, further highlighting significant irregularities and deconstruction of the SEI layer (Figure 9p).

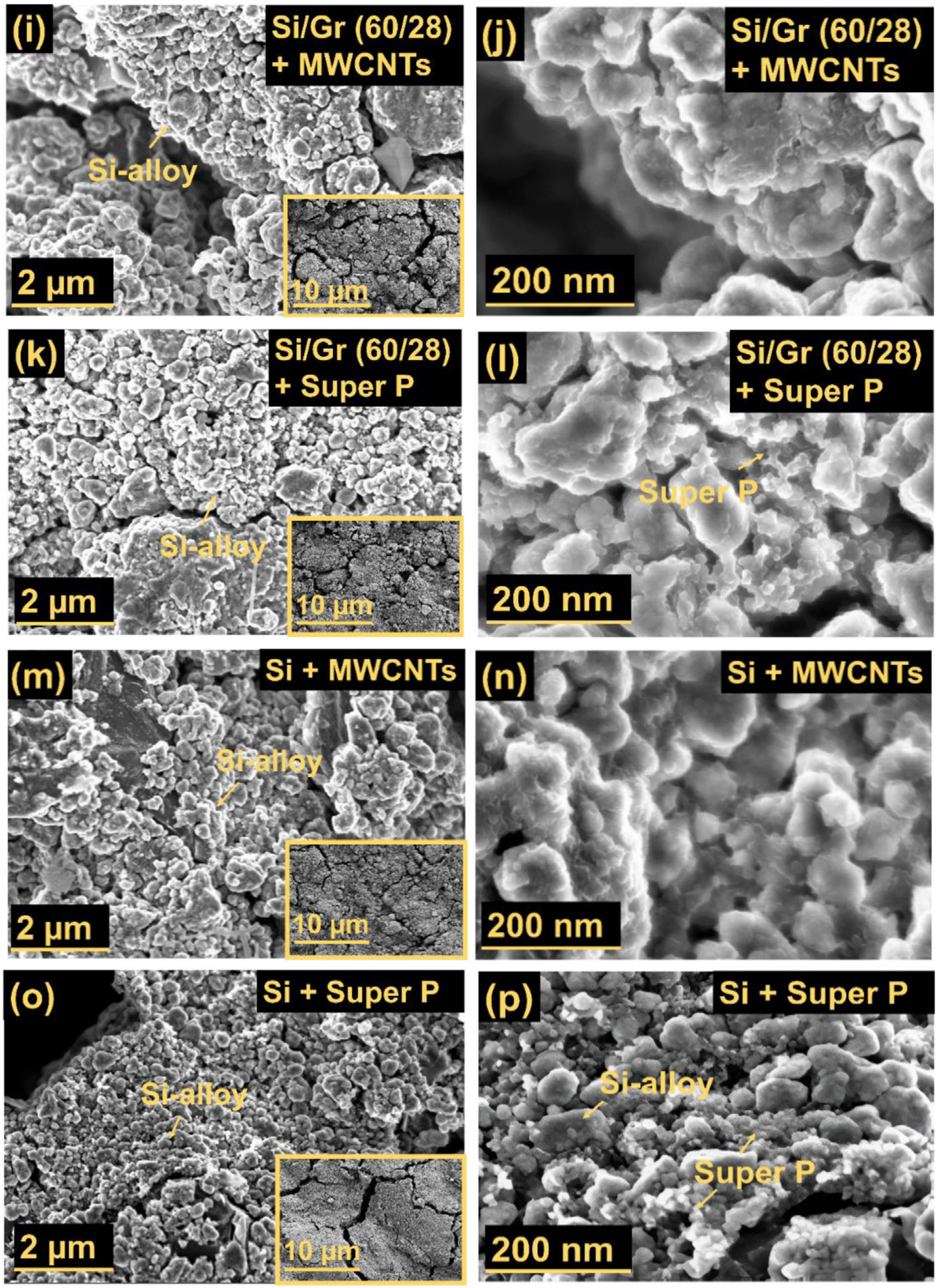

Figure 9. *Continued*

To investigate the structural changes after cycling, RAMAN measurements were performed as depicted in **Figure 12** a–d. Calculated R values for both cycled and non-cycled negative electrodes are presented in Figure 12e,f.

After cycling, the R values for MWCNTs-containing electrodes decrease, indicating a more ordered structure (Figure 12e,f). Several mechanisms may contribute to this behavior, including surface and bulk stabilization due to reactions between Li-ions and functional groups at defects, dangling bonds, and stress-induced atomic rearrangements. **Figure 13** shows the reaction mechanism during the lithiation process. One possible mechanism is that Li-ions interact with carboxylate groups ($-COO^-$) of MWCNTs, resulting in the formation of a MWCNTs–COO^-–Li^+–Si linkage. This can neutralize negative charges and lower localized charge density, reducing electron scattering and thereby decreasing the D-band intensity in RAMAN spectra. Additionally, Li-ion coordination may promote electronic delocalization within the MWCNTs network, enhancing structural order and further suppressing the D band.

Another factor contributing to the reduced R (I_D/I_G) value could be the reductive lithiation of carboxylate groups, leading to the formation of carboxyl species. These species can

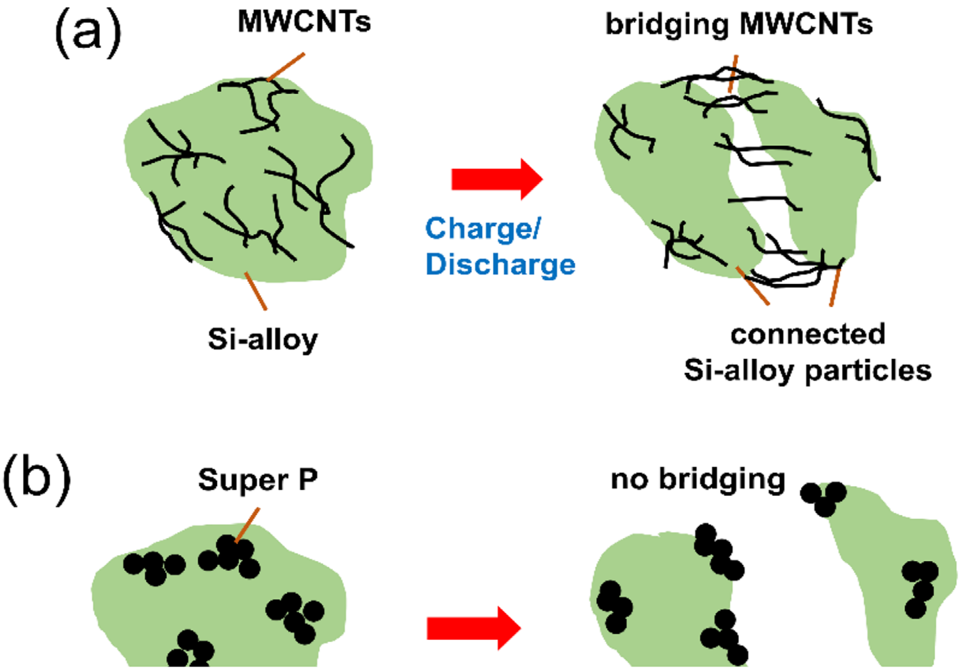

Figure 10. Effect of conductive additives on Si-alloy particle integrity during cycling: a) MWCNTs-based system, and b) Super P.

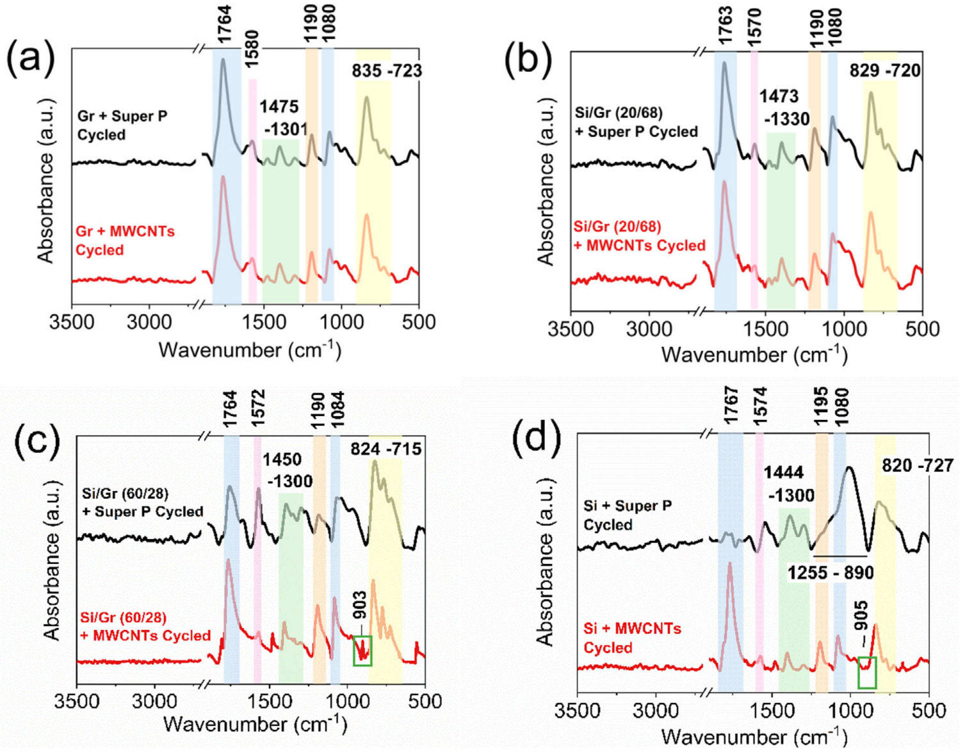

Figure 11. ATR-FTIR results of cycled: a) Gr + MWCNTs and Gr + Super P;b) Gr-rich Si/Gr (20/68) + MWCNTs and Gr-rich Si/Gr (20/68) + Super P; c) Si-rich Si/Gr (60/28) + MWCNTs and Si-rich Si/Gr (60/28) + Super P; d) Si + MWCNTs and Si + Super P negative electrodes.

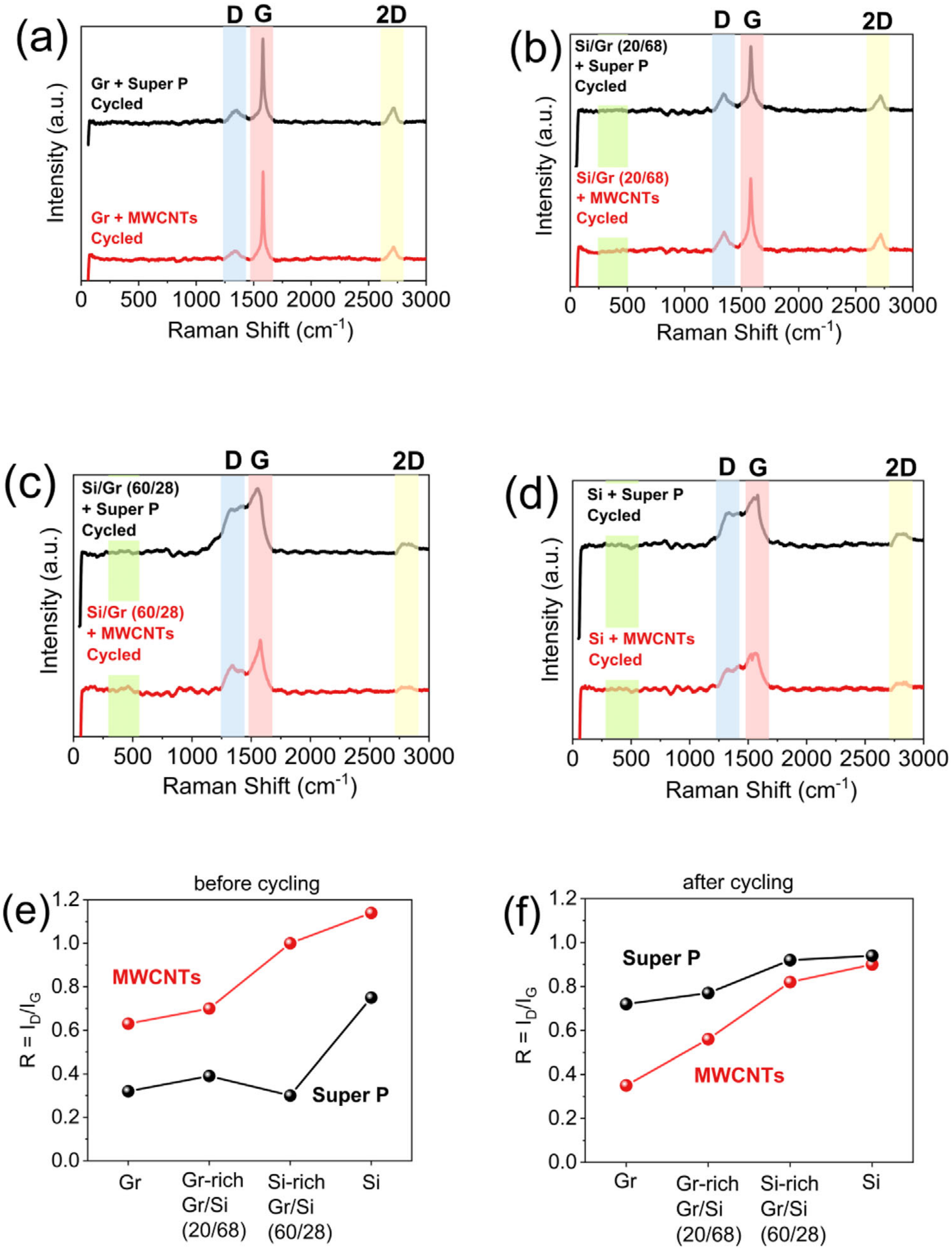

Figure 12. RAMAN spectroscopy results of cycled: a) Gr + MWCNTs and Gr + Super P; b) Gr-rich Si/Gr (20/68) + MWCNTs and Gr-rich Si/Gr (20/68) + Super P; c) Si-rich Si/Gr (60/28) + MWCNTs and Si-rich Si/Gr (60/28) + Super P, d) Si + MWCNTs and Si + Super P negative electrodes. Comparative R (ID/IG) estimations of all negative electrode formulation systems at their e) non-cycled; and f) cycled state.

decompose with CO_2 release, breaking the MWCNTs–O–Si linkage. The highly reactive Si surface can react with H_2O to form Si–OH, which can further condense with functional groups on MWCNTs, forming stable Si–O–C linkages. Such linkages can enhance the mechanical integrity of the composite structure and promote structural stability during cycling. In contrast, when Super P is used asa conductive additive, a decrease in the R value after cycling is not observed. Instead, all electrode systems with Super P exhibit an increase in R value (Figure 12e,f). This can be attributed to the inherently disordered nature of Super P, where cycling induces structural degradation, electrolyte decomposition, or irreversible reactions that introduce additional defects. These defects increase the R value and signal a loss of structural order. By comparison, in MWCNTs, defects, dangling bonds, and related reactive sites are often neutralized or saturated during cycling, leading to a lower R value.

Overall, the presence of oxygen-containing functional groups such as carboxyl (–COOH), hydroxyl (–OH), and carbonyl (–CO) on MWCNTs plays a multifaceted role in electrode performance. Theysignificantly enhance interfacial adhesion between (a) MWCNTs and binders (e.g., CMC, LiPAA), (b) MWCNTs and active materials (e.g., Si, Gr), and (c) MWCNTs and the

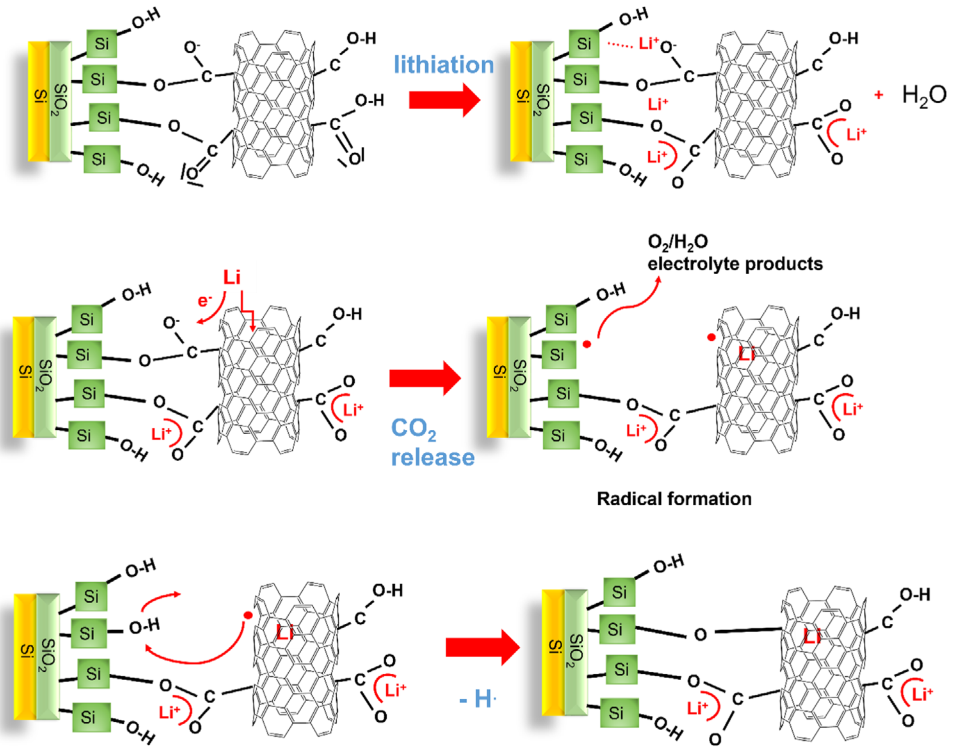

Figure 13. Interaction of Si/MWCNTs with Li-ions during the lithiation step.

current collector through binder mediation. This adhesion arises primarily from hydrogen bonding and covalent interactions between –COOH/–OH groups on MWCNTs and complementary functional groups on binders, as well as surface oxides on active materials. The resulting strong interfacial coupling enhances the mechanical integrity of the electrode film, prevents particle detachment during cycling, and mitigates delamination and cracking, particularly in high-volume-change systems such as Si-rich electrodes.

The improved cycling stability of Si negative electrodes withdefiect-mediated MWCNTs conductive additive arises from the MWCNT's ability to maintain mechanical and electrical integrity during repeated lithiation and delithiation. Oxygen-containing functional groups (e.g., –COOH, $–COO^-$, –OH) facilitate strong chemical bonding with both the binder and the native SiO_x layer on Si particles, ensuring robust interfacial adhesion. This anchoring effect prevents particle isolation despite the large volume changes of Si, allowing the CNT network to remain intact and conductive over cycling. While functionalization may initially reduce the intrinsic electronic conductivity of MWCNTs, the preservation of the percolation network throughout cycling outweighs this drawback which result in superior capacity retention compared to electrodes with Super P.

2.3. Full-Cell Tests

To validate the results obtained in half-cell configuration and assess their potential for practical applicability, electrochemical tests were performed in full-cells. From a practical perspective, full-cells were assembled only for the Si/Gr blended-based negative electrode materials. Due to the limited Li-ion availability in full-cell set-ups, the impact of conductive additives is expected to be reflected in the overall performance of the cell. **Figure 14a,b** displays the cycling performance of full-cells constructed with MWCNTs and Super P-containing Gr-rich Si/Gr (20/68) and Si-rich Si/Gr (60/28) negative electrodes coupled with $LiNi_{0.6}Mn_{0.2}Co_{0.2}O_2$ (NMC_{622}) positive electrode. To better understand the impact of MWCNTs in both Si/Gr-based full-cells, long-term cycling, Accumulated Irreversible Capacity (Q_{AIC}),[75] Accumulated Coulombic Inefficiency (Q_{ACIE}),[75] differential capacity (dQ/dV) and rate capability (power) tests are presented and discussed below.

As can be seen from Figure 14a, MWCNT and Super P-containing Gr-rich Si/Gr (20/68) electrode-based full-cells demonstrate comparable features up to 200 cycles. The ICE for both battery cells is almost similar, ≈80.6% for MWCNTs-based design and ≈80.9% for the Super P-based one. However, after the 120th cycle, a decline in long-term CE is obtained for Gr-rich Si/Gr (20/68) + MWCNTs-based cell, which is probably attributed to an unstable SEI layer resulting from the incompatible interaction between the functional groups of MWCNTs and that of Gr. The less stabilized interface between Gr and MWCNTs could trigger further parasitic reactions that lead to reduced CE. Q_{AIC} and Q_{ACIE} plots (Figure 14c,d) demonstrate that there are no significant differences between battery cells built from both MWCNTs and Super P-containing negative electrodes.

A slightly reduced specific discharge capacity up to the 80th cycle is observed for Si-rich Si/Gr (60/28) + MWCNTs-based battery cell as compared with its counterpart Super P (Figure 14b).

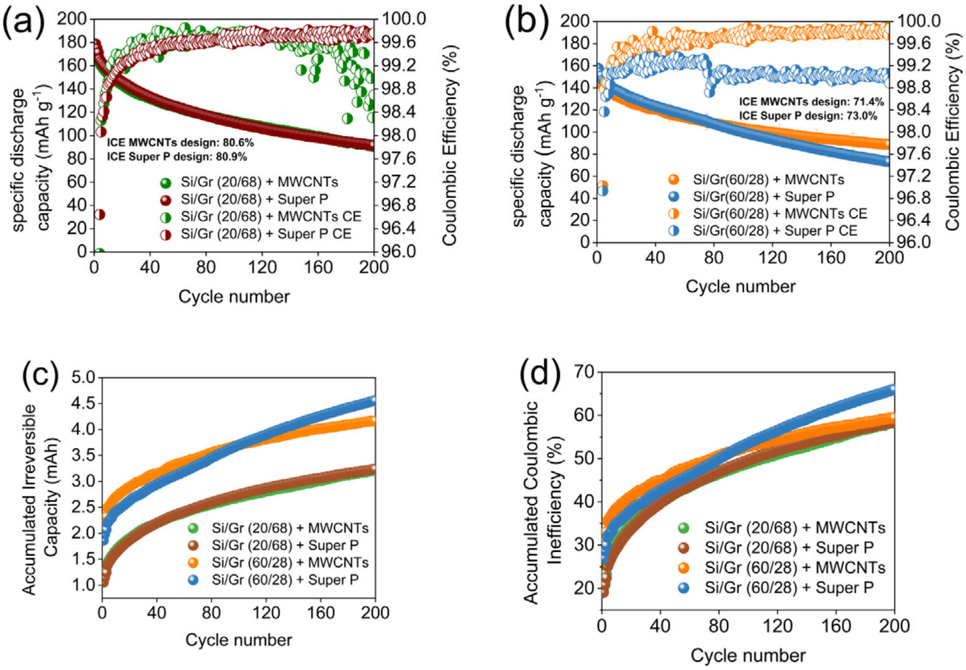

Figure 14. a,b) Full-cell cycling performance results; c,d) QAIC and QACIE of MWCNTs and Super P-containing Gr-rich Si/Gr (20/68) and Si-rich Si/Gr (60/28) negative electrode-based battery cells.

Further underlying this, an increased Q_{AIC} (Figure 14c) and Q_{AICE} (Figure 14d) are detected until 80th cycle. Afterward, however, up to 200th cycle, the specific discharge capacity of MWCNTs-based cell becomes enhanced (88.8 ± 7.2 mAh g^{-1}, at 200th cycle) compared to the Super P-based cell (73.1 ± 2.4 mAh g^{-1}). The higher consumption of Li-ions up to 80th cycle may be due to pre-storage of Li-ions that can lead to improved cycling stability and CE in later cycles. The ICE is found to be slightly lower for MWCNTs-based battery cell design (≈71.4%) as compared to Super P (≈73.0%), in line with results obtained in half-cells (Figure 7a–d). Despite lower ICE, the Si-rich Si/Gr (60/28) + MWCNTs-based battery cell, however, exhibits improved CE compared to the Si-rich Si/Gr (60/28) + Super P-based cell over a long-term cycling (i.e., up to the 200th cycle). For instance, at the 200th cycle, CE is found to be ≈99.8% for the MWCNTs-containing Si/Gr-based cell, while for its Super P counterpart, the CE is much lower (≈ 98.9%). Results from Q_{AIC} and Q_{AICE} (Figure 14c,d) corroborate the above observations in that, after the 80th cycle, the accumulated irreversible capacity loss and accumulated coulombic inefficiency are found to be higher for the Super P cell (4.6 mAh, ≈66%) compared to MWCNTs-based battery cell (4.1 mAh, ≈60%).

To gain deeper insights into the electrochemical behaviour and battery cell performance, differential capacity (dQ/dV) curves are presented in **Figure 15**.

The observed peak shifts in the dQ/dV analysis of full-cells can be attributed to several potential factors. One possibility is that the loss of Li-ions shifts the positive electrode's working potential due to a change in the operating window, a phenomenon that is unique to full-cells since half-cells have a relatively fixed potential of ≈0 V vs. Li/Li$^+$. When the operating window shifts due to Li-ion loss, the positive electrode's potential is elevated, causing all dQ/dV peaks for (de-)lithiation to shift to lower potentials. Another driving reason lies in the development of overpotentials within the battery cell itself, primarily due to the formation of SEI that limits the Li-ion transport. As overpotentials increase, the lithiation peak of the negative electrode (during charging) could shift to higher potentials, while discharging peaks to lower potentials, particularly given the relatively high current of C/5. While no significant differences in peak position or intensity are observed at different cycling stages in the Gr-rich Si/Gr (20/68) cell system, the Si-rich Si/Gr (60/28)-based cell exhibits notable differences when using different conductive additives (Figure 15). For the Si-rich Si/Gr (60/28) + MWCNTs negative electrode-based cell (Figure 15c), the peaks in the charging direction (top) shift toward higher potentials with an increasing cycle number. In the discharging direction (bottom), no peak shift is observed for cycles 10 and 50, suggesting the increase in overpotential and subsequent SEI build-up occurs at least partially during these cycles. However, for higher cycle numbers, a shift to higher potentials is observed in both charging and discharging, indicating a change in the aging behaviour. For Si-rich Si/Gr (60/28) + Super P negative electrode-based cells, all peaks are shifted to higher potentials, indicating that Li-ion loss predominates throughout all cycles (Figure 15d). This could be due to the Li-ion loss due to the continuous resistive SEI formation. These observations align well with the full-cell cycling results (Figure 14b), where MWCNTs-containing negative electrode-based battery cells show faster capacity loss at low cycle numbers compared to their Super P counterpart. This initial capacity loss is likely attributed to SEI formation in the case of the MWCNTs system. However, with higher cycle numbers, the earlier formed SEI helps mitigate further decomposition reactions, slowing down capacity fade and thus maintaining the higher capacity. In the of Super P-based

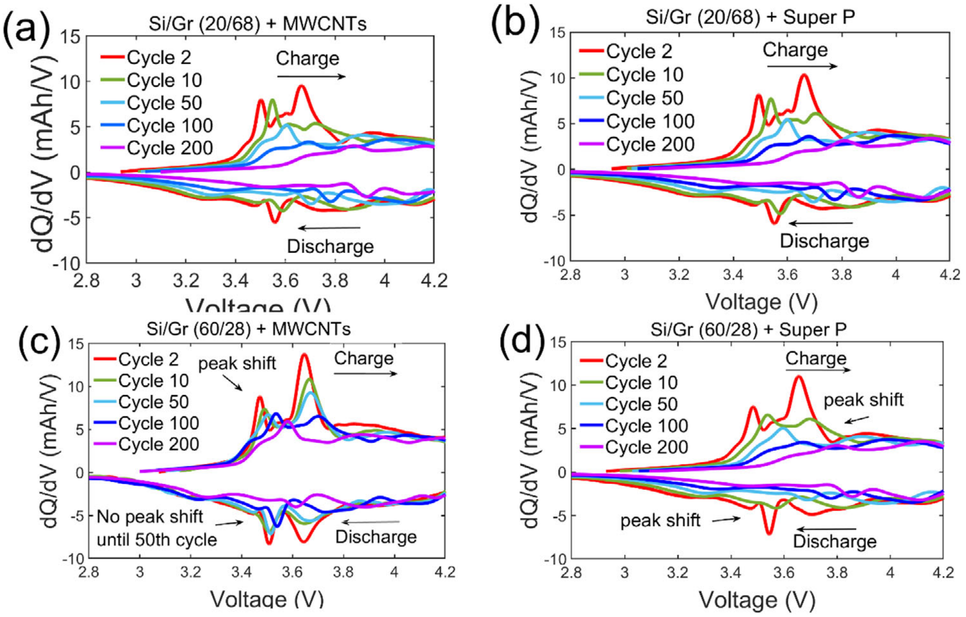

Figure 15. dQ/dV curves of Gr-rich Si/Gr (20/68) and Si-rich Si/Gr (60/28) negative electrode-based cells comprising MWCNTs or Super P.

cell system, a stable SEI does not form during the initial cycles, resulting in continued decomposition and accelerated capacity fade. **Figure 16** shows the rate capability test at various C-rates (C/10, C/5, C/2, 1C, 2C).

As shown in Figure 16 a, no significant difference in power output is observed between MWCNTs and Super P in Gr-rich Si/Gr (20/68) electrode-based full-cells across various C-rates, indicating that MWCNTs offer no additional benefit in graphite-dominated systems. In contrast, in the Si-rich Si/Gr (60/28) electrode-based battery cell system (Figure 16b), MWCNTs significantly enhance the electrical performance at higher C-rates (C/5 to 2C), indicating a strong positive impact on the power output in Si-rich electrode systems. This improvement can be attributed to several factors: 1) MWCNTs form a continuous percolating network that bridges isolated or fractured Si particles, ensuring efficient electron transport, one of the critical challenges for pure Si and Si-rich electrodes and thus reduces internal resistance under high current densities; 2) defect-rich MWCNTs promote improved interfacial contact through defect-mediated interactions that enhance wettability and lead to stronger adhesion to Si surfaces and thus better compatibility with the binder and electrolyte. These features facilitate both electronic and ionic transport, particularly in pure Si and Si-rich which are endowed with slow diffusivity. Furthermore, the surface defects in MWCNTs promote Li-ion adsorption and enable interfacial ion transport, and also lead toward enhancing electrolyte wetting and active Li^+ ion accessibility. In contrast, Super P lacks mechanical resilience and fails to maintain conductive pathways during Si expansion. Its point-to-point contact network is easily disrupted, resulting in poor electronic connectivity, elevated internal resistance and a significant decline in rate capability under high C-rate conditions.

3. Conclusion

This study presents a comparative analysis of MWCNTs and Super P as electrode conductive additives in Si-based anode materials and graphite as a benchmarking electrode material in Li-ion Batteries. It aims at appraising their impact on battery cell performance and cycling efficiency as well as an in-depth

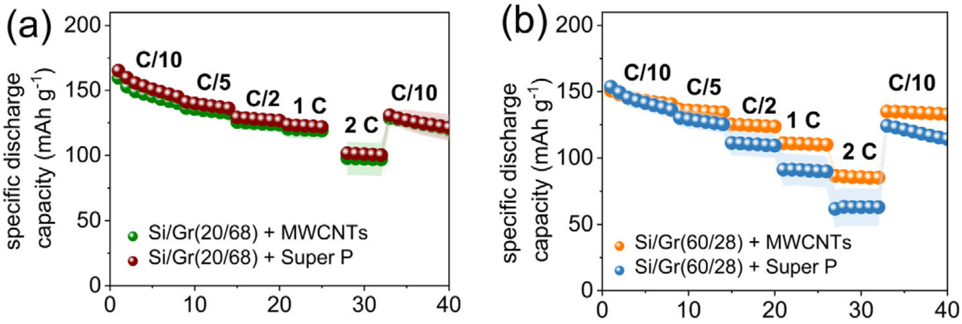

Figure 16. Rate capability results of Gr-rich Si/Gr (20/68) and Si-rich Si/Gr (60/28) negative electrode-based cells comprising MWCNTs or Super P.

Table 2. Negative electrode composition.

Negative Electrode	wt.% of electrode components					
	Super P	MWCNTs	Si	Gr	CMC	LiPAA
Gr + MWCNTs	–	2	–	88	10	–
Gr + Super P	2	–	–	88	10	–
Gr-rich Si/Gr (20/68) + MWCNTs	–	2	20	68	7.7	2.3
Gr-rich Si/Gr (20/68) + Super P	2	–	20	68	7.7	2.3
Si-rich Si/Gr (60/28) +MWCNTs	–	2	60	28	3.2	6.8
Si-rich Si/Gr (60/28) + Super P	2	–	60	28	3.2	6.8
Si + MWCNTs	–	2	88	–	–	10
Si + Super P	2	–	88	–	–	10

understanding of the underlying mechanisms. Defect-rich MWCNTs demonstrated significant improvement in electrochemical performance when combined with Si-rich Si/Gr blends and pure Si in half-cell configuration, resulting in enhanced reversible discharge capacity and capacity retention at the 100th cycle. Specifically, the MWCNTs-based pure Si electrode achieved a discharge capacity of 710.8 ± 19.9 mAh g^{-} and a capacity retention of 71.7%, while in the Si-rich Si/Gr (60/28) blend, it showed a reversible capacity of 534.2 ± 21.1 mAh g^{-} and a capacity retention of 73.3%. In comparison, the Super P-containing electrodes showed lower performance (pure Si: 422.8 ± 5.5 mAh g^{-} and 55.6%; Si-rich Si/Gr (60/28): 436.1 ± 16.3 mAh g^{-} and 61.7%). However, in pure Gr and Gr-dominated Si/Gr electrode systems, the benefits of MWCNTs are not as significant as in pure Si and Si-dominated Si/Gr electrode systems. Post-mortem analysis, including SEM, ATR-FTIR, and RAMAN spectroscopy, provided insights into surface chemistry and morphology of the electrodes before and after cycling, indicating that a more stable SEI layer formed on MWCNTs-containing Si and Si-rich Si/Gr blend electrodes sustains long-term cycling. This stability was also reflected in the full-cell tests, where Si-rich MWCNTs-containing Si/Gr-based cells demonstrated significantly improved cyclability and CE compared to their Super P counterparts. After 200 cycles, full-cells based on MWCNTs-containing Si-rich Si/Gr negative electrode demonstrate a specific discharge capacity of 88.8 ± 7.2 mAh g^{-1} and Coulombic Efficiency (CE) of 99.8%, whereas Super P-containing Si-rich Si/Gr-based cell presents a reduced discharge capacity of 73.1 ± 2.4 mAh g^{-1} and a lower CE of 98.9% after 200 cycles. However, no notable differences were observed in Gr-rich Si/Gr blend-based cells.

Overall, this study highlights the advantages of MWCNTs as an electrode conductive additive for Si-rich negative electrode-based lithium-ion battery cells, outperforming the state-of-the-art Super P in terms of cycling stability, capacity retention, rate capability, and CE. This is attributed to the unique interactions between the functional groups of defect-rich MWCNT and those of Si and Si-rich Si/Gr active materials as well as polymeric binders (CMC and LiPAA). These results open a new avenue toward realizing Si-rich negative electrode-based LIBs, however, more advanced characterizations, such as using XPS, NMR, GC-MS, etc., are needed to foster an in-depth mechanistic understanding, including decoupling the accompanying competitive interactions.

4. Experimental Section

Materials and Negative Electrode Production: In total, four different negative electrode systems (pure Gr, Gr-rich Si/Gr blend, Si-rich Si/Gr blend, and pure Si negative electrodes) were formulated (**Table 2**), each with MWCNTs or Super P as an electrode conductive additive. Graphite (Gr, MagE3, Hitachi Japan, 350 mAh g^{-1} reversible capacity, 22.9 µm particle size) and Si-alloy (Si, 3M, ≈1240 mAh g $^{-1}$ reversible capacity, particle size distribution in the range of 0.9 – 24 µm, surface area ≈6 m^2 g^{-1}) as active materials, 10 wt.% lithium poly(acrylic acid) LiPAA in H_2O and sodium carboxymethyl cellulose (CMC, WALOCEL) as polymeric binders, Carbon Black (Super P, IMERYS TIMCAL) and Tangled Multi-Walled Carbon Nanotubes (MWCNTs, Graphistrength CW2-L, Arkema) as electrode conductive agents were employed. The MWCNTs material was a water-based dispersion with 45.45 wt.% of MWCNTs and 54.55 wt.% of CMC. The LiPAA binder was produced by stirring poly (acrylic acid) (PAA, 25 wt.% of aqueous solution, $M_w = 240.000$, Acros Organics) in deionized water. 80% of the stoichiometric amount of lithium hydroxide monohydrate ($LiOH \cdot H_2O$, battery grade, Alfa Aesar) was added to the solution and heated up to 60°C. The solution was stirred overnight to obtain a 10 wt.% of LiPAA in water. The pH value was targeted at 7, and $LiOH \cdot H_2O$ was added if necessary (if the solution was still acidic, reaching a pH value of 7).

Si/Gr blend negative electrodes were produced using a three-step process, whereas the reference (pure) Gr and Si negative electrodes were made in a single step. For the production of Si/Gr blend, electrode components were mixed in 60 mL cups using a planetary micro mill (Pulverisette 7, Fritsch). A mixture of 10 wt.% LiPAA in H_2O was added to Si and mixed for 10 min at 800 rpm. Afterward, electrode conductive agents and CMC were added to the mixture and further mixed for 10 min. CMC has been established as an effective binder for Gr due to its favourable interaction with graphitic surfaces, whereas LiPAA can accommodate the significant volume changes of Si through the formation of robust bonds with the native SiO_x layer. Hamzelui et al. have demonstrated that adjusting the LiPAA/CMC ratio to match the Si/Gr composition enhances adhesion, maintains electronic connectivity, and results in superior electrochemical performance.[49] In line with this, the LiPAA/CMC binder ratio in this study was adjusted to match the Si/Gr composition. Finally, Gr was added, and the slurry was mixed for 20 min. For pure Gr negative electrode formulation with MWCNTs or Super P as conductive additives, all components were mixed for 1h at 800 rpm. In this case, only CMC was used as a binder. For the production of a pure Si negative electrode, the same procedure was conducted with only using 10 wt.% LiPAA in H_2O as a binder. The slurries were coated onto 14 µm thick electro deposited (ED) copper foil (Cu, CustomCells) using a sheetwise coating unit (CUF 5, SUMET, Germany). The coated films were dried at room temperature (22-26°C) for 24h. Afterward, electrodes were calendered at 10 N mm^{-1} in a laboratory calender pressure (SUMET, Germany), which were then punched using a high-precision electrode cutter (EL-CELL) with dimensions of 16 mm, and then dried overnight at 80°C in a vacuum oven (Buechi, Glass oven B-585 Drying). Table 2 presents the composition of the fabricated negative elctrodes.

Coin Cell Set-Up and Electrochemical Testing: CR2032 type coin half-cells were built in an argon-filled glove box ($O_2 < 1$ ppm, $H_2O < 0.1$ ppm) using Lithium metal chips (15.6 mm diameter, Gelon, China) as counter electrode and Si and Gr – based active materials as working electrodes, a glass fiber GF/C Whatman separator (17 mm diameter) and 90 µL of electrolyte (1.2 M $LiPF_6$ in EC: EMC (3:7, w/w) + 10 wt.% FEC, E-lyte). For full-cell configuration, Gr-rich Si/Gr (20/68) and Si-rich Si/Gr (60/28) were paired with 2.4 mAh cm^{-2} (12.5 mg cm^{-2}) and 3 mAh cm^{-2} (16 mg cm^{-2}) cathodes ($LiNi_{0.6}Mn_{0.2}Co_{0.2}O_2$, NMC622). Electrochemical testing was conducted using Neware BTS4000-5 V10 mA. The half-cells were cycled at C/10 in a voltage range of 0.01 – 0.9 V until 100 cycles. The full-cells were cycled in a voltage window of 2.8 – 4.35 V with two initial formation cycles at C/20 in CC charge and CC discharge mode. Afterward, they were cycled in the same mode at C/5 for up to 200 cycles. For rate capability tests, full-cells were cycled using the same voltage range at various C-rates (C/10, C/5, C/2, 1 C, and 2 C).

Analytical Techniques: Different analytical methods, namely SEM, ATR-FTIR, and RAMAN spectroscopy were used to characterize the surface chemistry of as-prepared (non-cycled) and cycled negative electrodes. For ATR-FTIR and Raman spectroscopies, cycled electrodes (vs. Li/Li^+, 30th cycle) were washed with DMC to remove traces of residual salts and dried under vacuum for 1h. The electrodes were sealed in an aluminium pouch back and transferred to a dry room (Dew point ≈ –55 °C, Room Temperature = 22°C), where the spectroscopic tests were conducted. A Bruker spectrometer (Vertex 70) was used to conduct ATR-FTIR measurements on both non-cycled and cycled negative electrodes. The measurements were performed in an attenuated total reflection (ATR) mode within the frequency range of 4000 – 500 cm^{-1}. The spectra were obtained with a resolution of 4 cm^{-1} for 256 scans. The RAMAN spectra were obtained using a Bruker Senterra spectrometer with a 532 nm He—Ne laser. The micro-RAMAN measurements were conducted using a 50×magnification objective. Each spectrum was measured at 25 points arranged in a square with a 5 µm distance from each other. The average of these measurements was then calculated and utilized as a representative measure of a 25 µm^2 surface. Afterward, the spectra baseline corrected was corrected. Aiming to analyze the samples' morphologies, SEM was conducted on non-cycled and cycled electrodes utilizing a Zeiss Supra 55 apparatus at an acceleration voltage of either 5 or 10 kV.

Acknowledgements

Funded by the European Union under the greenSPEED project (Grant Agreement: 101069528). Views and opinions expressed are however those of the author(s) only and do not necessarily reflect those of the European Union or CINEA. Neither the European Union nor the granting authority can be held responsible for them.

Open access funding enabled and organized by Projekt DEAL.

Conflict of Interest

All authors declared that there are no conflicts of interest.

Author Contributions

L. Ü. conceived the ideas of the work and performed experimentation, data analysis, conceptualization (lead), interpretation, and wrote the original draft. V. M. F. took review and editing, SEM images. F. W. Review and editing. E. F. did supervision, project funder, conceptualization (support), review, and editing. G. G. E. performed data interpretation, supervision, review, and editing.

Data Availability Statement

The data that support the findings of this study are available from the corresponding author upon reasonable request.

Keywords

carbon nanotubes, conductive additive, SEI layer, lithium-Ion battery, silicon anode

Received: June 3, 2025
Revised: August 20, 2025
Published online: September 10, 2025

[1] S. Wolf, M. Lüken, in *Emerging Battery Technologies to Boost the Clean Energy Transition: Cost, Sustainability, and Performance Analysis*, Springer International Publishing, Cham, **2024**.
[2] L. Ünal, V. Maccio-Figgemeier, G. G. Eshetu, E. Figgemeier, *ChemElectroChem* **2024**, *11*, 202400146.
[3] L. Ünal, et al., *Adv. Mater. Interfaces* **2024**, *11*, 2400024.
[4] G. G. Eshetu, E. Figgemeier, *ChemSusChem*,*12*, 2515.
[5] G. G. Eshetu, H. Zhang, X. Judez, H. Adenusi, M. Armand, S. Passerini, E. Figgemeier, *Nat. Commun.* **2021**, *12*, 5459.
[6] W. Zhao, C. Zhao, H. Wu, L. Li, C. Zhang, *J. Energy Storage* **2024**, *81*.
[7] M. Winter, B. Barnett, K. Xu, *Chem. Rev.* **2018**, *118*, 11433.
[8] T. Placke, R. Kloepsch, S. Dühnen, M. Winter, *J. Solid State Electrochem.* **2017**, *21*, 1939.
[9] M. Obrovac, *Curr. Opin. Electrochem.* **2018**, *9*, 8.
[10] M. Ashuri, Q. He, L. L. Shaw, *Nanoscale* **2016**, *8*, 74.
[11] Z. Wang, M. Yao, H. Luo, C. Xu, H. Tian, Q. Wang, H. Wu, Q. Zhang, Y. Wu, *Small* **2024**, *20*, 2306428.
[12] X. Fan, T. Cai, S. Wang, Z. Yang, W. Zhang, *Small* **2023**, *19*, 2300431.
[13] C. Zhang, et al., *Small Struct.* **2021**, *2*, 2100009.
[14] P. Sehrawat, C. Julien, S. Islam, *Mater. Sci. Eng., B* **2016**, *213*, 12.
[15] S. Jessl, D. Beesley, S. Engelke, C. J. Valentine, J. C. Stallard, N. Fleck, S. Ahmad, M. T. Cole, M. De Volder, *Mater. Sci. Eng., A* **2018**, *735*, 269.
[16] B. J. Landi, M. J. Ganter, C. D. Cress, R. A. DiLeo, R. P. Raffaelle, *Energy Environ. Sci.* **2009**, *2*, 638.
[17] P.-X. Hou, C. Liu, H.-M. Cheng, *Carbon* **2008**, *46*, 2003.
[18] C. Gao, M. Guo, Y. Liu, D. Zhang, F. Gao, L. Sun, J. Li, X. Chen, M. Terrones, Y. Wang, *Carbon* **2023**, *212*, 118133.
[19] C. Gao, D. Gou, G. Huang, Z. Zhang, J. Wei, F. Gao, Y.i Zhang, M. Terrones, X. Chen, Y. Wang, *Nano Energy* **2025**, *138*, 110863.
[20] S. W. Schmidt, T. Christ, C. Glockner, M. K. Beyer, H. Clausen-Schaumann, *Langmuir* **2010**, *26*, 15333.
[21] S. Björklund, V. Kocherbitov, *Sci. Rep.* **2017**, *7*, 9960.
[22] L. A. Algharagholy, *J. Electron. Mater.* **2019**, *48*, 2301.
[23] M. Berahman, M. Taheri, M. Sheikhi, A. Zarifkar, in *2013 21st Iranian Conference on Electrical Engineering (ICEE)*, IEEE, New York, **2013**, 1, 10.1109/IranianCEE.2013.6599543.
[24] M. Ohnishi, T. Shiga, J. Shiomi, *Phys. Rev. B* **2017**, *95*, 155405.
[25] L.-I. Battery, *Adv. Sci* **2023**, *10*, 2207355.
[26] S. B. Park, M. S. Lee, M. Park, *Carbon Lett.* **2014**, *15*, 117.
[27] J. Chen, A. ? I. Minett, Y. Liu, C. Lynam, P. Sherrell, C. Wang, G. G. Wallace, *Adv. Mater.* **2008**, *20*, 566.
[28] H. Khalil, L. Nassar, V. S. Wadi, V. Naddeo, F. Banat, S. W. Hasan, in *Water-Energy-Nexus in the Ecological Transition: Natural-Based Solutions, Advanced Technologies and Best Practices for Environmental Sustainability*, Springer, Cham, **2022**.

[29] Y. Dall'Agnese, Université Paul Sabatier – Toulouse III, 2016TOU30025, **2016**. [Online]. Available: https://theses.hal.science/tel-01452608.
[30] P. Florek, M. Król, P. Jeleń, W. Mozgawa, *Materials* **2021**, *14*, 1835.
[31] V. Ţucureanu, A. Matei, A. M. Avram, *Crit. Rev. Anal. Chem.* **2016**, *46*, 502.
[32] A. Ramya, B. Manoj, A. N. Mohan, *Asian J. Chem.* **2016**, *28*, 1031.
[33] P. Kargl, V. Drews, P. Daubinger, O. Schweighofer, M. Marinaro, G. A. Giffin, M. Wohlfahrt-Mehrens, A. Thaler, *J. Power Sources* **2022**, *548*, 232042.
[34] V. L. Chevrier, L.i Liu, D. B.a Le, J. Lund, B. Molla, K. Reimer, L. J. Krause, L. D. Jensen, E. Figgemeier, K. W. Eberman, *J. Electrochem. Soc.* **2014**, *161*, A783.
[35] R. Petibon, et al., *J. Electrochem. Soc.* **2016**, *163*, A1146.
[36] C. L. Berhaut, D. Z. Dominguez, P. Kumar, P.-H. Jouneau, W. Porcher, D. Aradilla, S. Tardif, S. Pouget, S. Lyonnard, *ACS Nano* **2019**, *13*, 11538.
[37] T. Vorauer, J. Schöggl, S. G. Sanadhya, M. Poluektov, W. D. Widanage, L. Figiel, S. Schädler, B. Tordoff, B. Fuchsbichler, S. Koller, R. Brunner, *Commun. Mater.* **2023**, *4*, 44.
[38] A. Oufakir, L. Khouchaf, M. Elaatmani, A. Zegzouti, G. Louarn, A. B. Fraj, *MATEC Web of Conferences* **2018**, *149*, 01041.
[39] R. Ellerbrock, M. Stein, J. Schaller, *Sci. Rep.* **2022**, *12*, 11708.
[40] R. Tian, X. Wang, M. Li, H. Hu, R. Chen, F. Liu, H. Zheng, L. Wan, *Appl. Surf. Sci.* **2008**, *255*, 3294.
[41] M. J. Rahman, T. Mieno, *J. Nanomater.* **2014**, *2014*, 2.
[42] M. Nawaz, S. Rauf, G. Catanante, M. Nawaz, G. Nunes, J. Marty, A. Hayat, *Sensors* **2016**, *16*, 1651.
[43] K. Takei, R. Takahashi, T. Noguchi, *J. Phys. Chem. B* **2008**, *112*, 6725.
[44] B. Smith, *Spectroscopy* **2016**, *3*, 28.
[45] Z. Wang, T. Huang, Z. Liu, A. Yu, *Electrochim. Acta* **2021**, *389*, 138806.
[46] E. H. Mejía, H. Contreras, E. Delgado, G. Quintana, *International Journal of Chemical Engineering* **2019**, *2019*, 3085691.
[47] L. Yadav, L. Yadav, *Organic spectroscopy* **2005**, 52.
[48] P. Li, G. Chen, Y. Lin, F. Chen, L. Chen, N. Zhang, Y. Cao, R. Ma, X. Liu, *Macromol. Chem. Phys.* **2020**, *221*, 1900414.
[49] N. Hamzelui, G. G. Eshetu, E. Figgemeier, *J. Energy Storage* **2021**, *35*, 102098.
[50] S. Costa, E. Borowiak-Palen, M. Kruszynska, A. Bachmatiuk, R. Kalenczuk, *Materials Science-Poland* **2008**, *26*, 433.
[51] I. Z. Gonzalez, H.-C. Chiu, R. Gauvin, G. P. Demopoulos, Y. Verde-Gomez, *Mater. Today Commun.* **2022**, *30*, 103158.
[52] L. Bokobza, J.-L. Bruneel, M. Couzi, *C* **2015**, *1*, 77.
[53] E. M. Dief, A. P. L. Brun, S. Ciampi, N. Darwish, *Surfaces* **2021**, *4*, 81.
[54] A. M. Schrader, J. I. Monroe, R. Sheil, H. A. Dobbs, T. J. Keller, Y. Li, S. Jain, M. S. Shell, J. N. Israelachvili, S. Han, *Proc. Natl. Acad. Sci. USA* **2018**, *115*, 2890.
[55] K. G. Gallagher, D. W. Dees, A. N. Jansen, D. P. Abraham, S.-H. Kang, *J. Electrochem. Soc.* **2012**, *159*, A2029.
[56] P.h. Bernardo, J.-M. Le Meins, L. Vidal, J. Dentzer, R. Gadiou, W. Märkle, P. Novák, M. E. Spahr, C. Vix-Guterl, *Carbon* **2015**, *91*, 458.
[57] M. Park, J.-u. Jang, J. H. Park, J. Yu, S. Y. Kim, *Polymers* **2020**, *12*, 997.
[58] Y. Wang, et al., *ACS Appl. Mater. Interfaces* **2024**, *16*, 67791.
[59] D. Aurbach, Y. Ein-Ely, A. Zaban, *J. Electrochem. Soc.* **1994**, *141*, L1.
[60] S. Ramesh, O. P. Ling, *Polym. Chem.* **2010**, *1*, 702.
[61] D. Aurbach, Y. Gofer, J. Langzam, *J. Electrochem. Soc.* **1989**, *136*, 3198.
[62] D. Aurbach, B. Markovsky, A. Shechter, Y. Ein-Eli, H. Cohen, *J. Electrochem. Soc.* **1996**, *143*, 3809.
[63] D. Aurbach, M. D. Levi, E. Levi, A. Schechter, *J. Phys. Chem. B* **1997**, *101*, 2195.
[64] D. Aurbach, M. Moshkovich, Y. Cohen, A. Schechter, *Langmuir* **1999**, *15*, 2947.
[65] N. Peruzzi, B. W. Ninham, P. Lo Nostro, P. Baglioni, *J. Phys. Chem. B* **2012**, *116*, 14398.
[66] D. Aurbach, Y. Gofer, M. Ben-Zion, P. Aped, *J. Electroanal. Chem.* **1992**, *339*, 451.
[67] C. C. Nguyen, S.-W. Song, *Electrochim. Acta* **2010**, *55*, 3026.
[68] J. Yang, N. Solomatin, A. Kraytsberg, Y. Ein-Eli, *ChemistrySelect* **2016**, *1*, 572.
[69] A. Xiao, L. Yang, B. L. Lucht, S.-H. Kang, D. P. Abraham, *J. Electrochem. Soc.* **2009**, *156*, A318.
[70] F. Shi, P. N. Ross, G. A. Somorjai, K. Komvopoulos, *J. Phys. Chem. C* **2017**, *121*, 14476.
[71] Z. Cao, X. Zheng, Y. Wang, W. Huang, Y. Li, Y. Huang, H. Zheng, *Nano Energy* **2022**, *93*, 106811.
[72] B. Hu, S. Jiang, J. Zhang, Z. Zhang, L. Zhang, *Electrochemical Society Meeting Abstracts* **2018**, *233*, 461.
[73] Z. Xu, J. Yang, T. Zhang, Y. Nuli, J. Wang, S.-i. Hirano, *Joule* **2018**, *2*, 950.
[74] L. Zhang, Y. Liu, Y. Wang, X. Li, Y. Wang, *Appl. Surf. Sci.* **2021**, *557*, 149838.
[75] F. Holtstiege, A. Wilken, M. Winter, T. Placke, *Phys. Chem. Chem. Phys.* **2017**, *19*, 25905.